



HAL
open science

Numerical simulation of surfactant-laden emulsion formation in an un-baffled stirred vessel

Fuyue Liang, Lyes Kahouadji, Juan Pablo Valdes, Seungwon Shin, Jalel Chergui, Damir Juric, Omar Matar

► **To cite this version:**

Fuyue Liang, Lyes Kahouadji, Juan Pablo Valdes, Seungwon Shin, Jalel Chergui, et al.. Numerical simulation of surfactant-laden emulsion formation in an un-baffled stirred vessel. *Chemical Engineering Journal*, 2023, pp.144807. 10.1016/j.cej.2023.144807 . hal-04172641

HAL Id: hal-04172641

<https://hal.science/hal-04172641>

Submitted on 27 Jul 2023

HAL is a multi-disciplinary open access archive for the deposit and dissemination of scientific research documents, whether they are published or not. The documents may come from teaching and research institutions in France or abroad, or from public or private research centers.

L'archive ouverte pluridisciplinaire **HAL**, est destinée au dépôt et à la diffusion de documents scientifiques de niveau recherche, publiés ou non, émanant des établissements d'enseignement et de recherche français ou étrangers, des laboratoires publics ou privés.

Numerical simulation of surfactant-laden emulsion formation in an un-baffled stirred vessel

Fuyue Liang^a, Lyes Kahouadji^a, Juan Pablo Valdes^a, Seungwon Shin^b, Jalel Chergui^c, Damir Juric^{c,d} and Omar K. Matar^a

^aDepartment of Chemical Engineering, Imperial College London, South Kensington Campus, London SW7 2AZ, United Kingdom

^bDepartment of Mechanical and System Design Engineering, Hongik University, Seoul 04066, Republic of Korea

^cUniversité Paris Saclay, Centre National de la Recherche Scientifique (CNRS), Laboratoire Interdisciplinaire des Sciences du Numérique (LISN), 91400 Orsay, France

^dDepartment of Applied Mathematics and Theoretical Physics, University of Cambridge, Centre for Mathematical Sciences, Wilberforce Road, Cambridge CB3 0WA, United Kingdom

ARTICLE INFO

Keywords:

Un-baffled stirred mixer
Two-phase flow
Surfactant
Mixing
LES

ABSTRACT

The present study aims to elucidate the interplay among the interfacial dynamics, surfactant transport, and underlying flow structure inside a cylindrical stirred vessel equipped with a pitched blade turbine. To address this, massively parallel three-dimensional, interface-tracking, large eddy simulation of oil-in-water dispersions are deployed to provide detailed, realistic visualisations of the intricate interfacial dynamics coupled to the turbulent flow field. In particular, we isolate the effect of surfactant arising from interfacial tension reduction and Marangoni stress (related to surfactant concentration gradient) by comparing two surfactant-laden systems, one being a realistic and experiment-achievable case, and another a simulation-exclusive system where the Marangoni stress is turned off. The comparison consists of qualitative interface visualisation as well as quantitative statistics in terms of dispersed phases counts and their size distribution. Finally, surfactant elasticity is modified with an aim of exploring its effect on the concerned mixing system.


1. Introduction

Given the heavy involvement of immiscible liquid mixing both in our daily life (e.g., food and cosmetics) and in high-end industrial applications (e.g., drug delivery), understanding the interfacial flows under highly dynamic conditions is of practical significance. Surface-active agents (surfactants) are commonly present within such systems, either by design or as contaminants, affecting both the mixing performance and the final quality of the mixed product. It is challenging to generalise the effect of surfactant in a mixing system as surfactant alters the interfacial behaviors in a complex manner that depends on surfactant distribution on the interface and its interphase transport with the bulk. In addition, the dynamic interfacial rheology (though beyond the scope of this work) in such system elevates the complexity of the roles played by surfactant. Consequently, surfactant could either suppress or enhance the drop deformation under dynamic flow, diverging the mixing metrics of interest, for instance, interfacial area and equilibrium drop size distribution. These challenges hamper the understanding and control of interfacial behaviours within a surfactant-laden mixing vessel, which is a prevalent scenario in industry.

However, only a few studies have aimed at understanding liquid dispersion in the presence of surfactant inside a stirred vessel; most of these studies have addressed the problem regarding the surfactant influence on the final drop sizes and their distribution, leaving a gap in our understanding of the underlying physical mechanisms governing the inter-

facial behaviours within such system. The earliest experiment to study the effect of surfactant on drop sizes is by Lee and Soong [1985] where five liquid-liquid systems and nine types of surfactants were examined. The authors found that the size of drops produced is smaller (relative to the one predicted using correlations based on clean liquid-liquid system) and more uniform (narrower drop size distribution). Later, Koshy et al. [1988] developed a drop breakup model to predict the maximum drop size at various surfactant concentrations arguing that the effect of surfactant on stirred-vessel emulsification is not only by the decrease in interfacial tension, but also through the generation of an interfacial tension gradient across the interface (and thus Marangoni stress, which, albeit, was not referred to as much in that study). Several subsequent studies have been carried out to expand knowledge in this field by considering surfactant concentration [Chatzi et al., 1991, El-Hamouz, 2007], rheological properties of surfactant-laden interface [Lucassen-Reynders and Kuipers, 1992], and the types of surfactant head group [Goloub and Pugh, 2003]. Groeneweg et al. [1994] have shown the appearance of a large number of mini-drops (a bimodal drop size distribution) for the surfactant-laden system, and rationalised that the phenomenon is due to surfactant-induced tip-streaming [Eggleton et al., 2001]. More related work has been on the surfactant effect on the flow field modification in a stirred vessel; interested readers can refer to Mishra et al. [1998], Arora et al. [2002], Mavros et al. [2011], Montante et al. [2011] and references therein.

Nevertheless, interfacial dynamics on a surfactant-laden interface has been well studied by investigating drop deformation subjected to a simple flow field, both in the case of

 fuyue.liang18@imperial.ac.uk (F. Liang)
ORCID(s): 0000-0002-4159-6993 (F. Liang)

60 insoluble [Stone and Leal, 1990, Milliken et al., 1993, Li
 61 and Pozrikidis, 1997, Eggleton et al., 1999, 2001, Bazhlekov
 62 et al., 2006, Feigl et al., 2007, Soligo et al., 2020a] and solu-
 63 ble surfactant [Milliken and Leal, 1994, Eggleton and Stebe,
 64 1998, Jin et al., 2006, Jin and Stebe, 2007], which leads
 65 to several reviews in this field (see, for example, Briscoe
 66 et al. [1999], Fischer and Erni [2007]). More recently, Soligo
 67 et al. [2019] carried out a direct numerical simulation of
 68 surfactant-laden drops dispersed in turbulent flow in which
 69 a clear interplay among local flow field (considering shear
 70 stress, Marangoni stress, and the effect of Weber number),
 71 surfactant concentration and dispersed phase morphology is
 72 displayed. In their subsequent work, Soligo et al. [2020b]
 73 studied the flow modification introduced by the surfactant-
 74 laden drop under the same flow conditions, in terms of ve-
 75 locity profiles, vorticity profiles, and a specifically-defined
 76 flow topology parameter [Perry and Chong, 1987].

77 The short review of the current literature reveals the rela-
 78 tive scarcity of information available on flow structure and
 79 interfacial dynamics in practical mixing units, such as stirred
 80 vessels, and more specifically, in the presence of surfactant.
 81 The present study attempts to elucidate the interplay among
 82 the interfacial deformation, surfactant transport, and under-
 83 lying flow structure inside a cylindrical un-baffled stirred
 84 vessel equipped with a pitched blade turbine. The configu-
 85 ration of the vessel adapted here is partially inspired by
 86 the recent investigation performed by Busciglio et al. [2014,
 87 2016], where the authors showed the potential of the un-
 88 baffled stirred vessel as a viable alternative to the baffled
 89 one. This is in contrast to the view held more commonly
 90 that un-baffled stirred vessels are generally less efficient than
 91 their baffled counterparts, which led to the former being less
 92 well-studied and their flow and interfacial dynamics less well
 93 explored.

94 The underlying physics governing the interfacial dynam-
 95 ics in the presence of soluble surfactant is modelled accu-
 96 rately thanks to a hybrid front-tracking/level-set algorithm
 97 [Shin et al., 2018], which has been extensively validated in
 98 previous studies [Constante-Amores et al., 2021a,b, Liang
 99 et al., 2022]. Combined with this, the massively parallel,
 100 three-dimensional, large eddy simulations [Shin et al., 2017]
 101 of oil-in-water emulsification are deployed to provide de-
 102 tailed, realistic visualisations of the interfacial dynamics cou-
 103 pled to the turbulent flow field, from the onset of impeller
 104 rotation through to a state where up to 30 revolutions have
 105 completed.

106 The following section (Section 2) will briefly introduce
 107 the simulation technique and the governing equations. Sec-
 108 tion 3 discusses the effect of surfactant on the mixing pro-
 109 cess, decoupling the influence originating from the interfa-
 110 cial tension reduction and the Marangoni stress induced by
 111 the non-uniform surfactant distribution. Furthermore, we
 112 provide a parametric study of the surfactant elasticity (the
 113 sensitivity of interfacial tension to the surfactant concentra-
 114 tion). Finally, concluding remarks, and suggestions for pos-
 115 sible future work will be provided in Section 4.

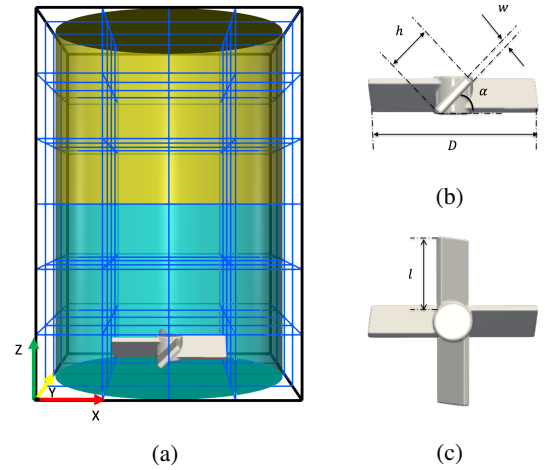


Figure 1: (a) Schematic illustration of the computational domain for the oil-water mixing system: a stirred vessel, equipped with a 4-pitched-blade turbine, is filled with oil in the upper-half (coloured in gold) and water below (coloured in blue); the blades have length l , width h , and thickness w , and are inclined at an angle α to the horizontal. The computational domain is divided into $4 \times 4 \times 6$ subdomains. The number of the Cartesian structured grids per subdomain is 64^3 , which gives a total grid number of $256 \times 256 \times 384$; (b) - (c) display side- and top-views of the turbine, respectively.

2. Problem Formulation

2.1. Simulation configuration and technique

The configuration considered in this work is shown in Figure 1. It is composed of a cylindrical vessel of diameter $T = 8.5$ cm and height $H = 12.75$ cm, filled with water in the lower half and an overlaying oil phase above (volume fraction of oil, $\phi = 0.5$). The viscosity ratio of two liquids is 5.4. The impeller employed is a pitched blade turbine (PBT), which is immersed in the water phase. Details of the impeller geometry and the physical properties of two phases are listed in Table 1.

2.2. Governing equations

With the purpose of studying the dynamics of surfactant-laden multiphase mixing inside the stirred vessel, we solved the two-phase Navier-Stokes equations in a Cartesian domain $\mathbf{x} = (x, y, z) \in [0, 8.6]^2 \times [0, 12.5]$ cm³, as in our previous work [Liang et al., 2022] but, additionally, interfacial tension alternation is considered:

$$\nabla \cdot \bar{\mathbf{u}} = 0, \quad (1)$$

$$\rho \left(\frac{\partial \bar{\mathbf{u}}}{\partial t} + \bar{\mathbf{u}} \cdot \nabla \bar{\mathbf{u}} \right) = -\nabla \bar{p} + \nabla \cdot \left[(\mu + \rho C_s^2 \Delta^2 |\bar{S}|) (\nabla \bar{\mathbf{u}} + \nabla \bar{\mathbf{u}}^T) \right] + \rho \mathbf{g} + \mathbf{F}_{\text{fsi}} + \int_{A_e} [\sigma \kappa \mathbf{n} + \nabla_s \sigma] \delta_f(\mathbf{x} - \mathbf{x}_f) dA_e. \quad (2)$$

In Eq. (2), $\bar{\mathbf{u}}$ and \bar{p} are respectively the ensemble-averaged velocity and pressure; \mathbf{g} is the gravitational acceleration. The

Table 1

Detailed geometry of the impeller and physical properties of the two phases.

Impeller Geometry [cm]	
diameter, D	4.25
height, h	1
thickness, w	0.2
length, l	2.5
clearance, C	1
inclined angle, α [°]	45
rotation speed, N [rps]	5
Physical properties	
surfactant-free interfacial tension, σ_s [Pa·m]	0.035
oil viscosity, μ_o [Pa·s]	5.4×10^{-3}
water viscosity, μ_w	1.0×10^{-3}
oil density, ρ_o [kg/m ³]	824
water density, ρ_w	998

respectively, where \mathbf{u}_t is the tangential velocity vector on the interface, which is computed from the interface velocity, \mathbf{u}_s , via $\mathbf{u}_t = (\mathbf{u}_s \cdot \mathbf{t}) \mathbf{t}$, with \mathbf{t} being the unit vector tangential to the interface. The first term on the right corresponds to interface diffusion, and D_s is the surfactant diffusivity in the plane of the interface; J accounts for the mass flux from the bulk. In general, the flux from the bulk is determined by surfactant adsorption which could be divided into two time-dependent processes: the diffusion of surfactant from the bulk phase (diffusion flux, J_{diff}) and the adsorption onto the interface (adsorption/desorption flux, $J_{\text{a/d}}$). Firstly, $J_{\text{a/d}}$ can be written as:

$$J_{\text{a/d}} = k_a C_{\text{sub}} (\Gamma_\infty - \Gamma) - k_d \Gamma, \quad (4)$$

where k_a and k_d are the kinetic coefficients for adsorption and desorption, respectively, and Γ_∞ is the saturation concentration on the interface; C_{sub} represents the surfactant bulk concentration evaluated at the layer immediately adjacent to the interface, which is known as the bulk ‘‘sub-phase’’. This sub-phase concentration is determined by diffusion from the bulk:

$$J_{\text{diff}} = -D_b \mathbf{n} \cdot \nabla C|_{\text{sub}}, \quad (5)$$

where D_b refers to the diffusivity in the bulk phase, and C is the surfactant concentration in the bulk which is governed by the convection-diffusion equation as follows:

$$\frac{\partial C}{\partial t} + \mathbf{u} \cdot \nabla C = D_b \nabla^2 C. \quad (6)$$

To satisfy conservation of surfactant, the diffusive flux from the bulk, Eq. (5), balances the kinetic sorptive flux, Eq. (4), and both mechanisms govern the flux to the interface [Eggleton and Stebe, 1998, Manikantan and Squires, 2020]. Hence,

$$J = J_{\text{a/d}} = J_{\text{diff}}. \quad (7)$$

When surfactant adsorbs onto the interface, the interfacial tension decreases from its clean surface value, σ_s . The Langmuir relation is used herein to describe such an effect:

$$\sigma = \sigma_s + \mathcal{R} T \Gamma_\infty \ln \left(1 - \frac{\Gamma}{\Gamma_\infty} \right) = \sigma_s \left[1 + \beta_s \ln \left(1 - \frac{\Gamma}{\Gamma_\infty} \right) \right], \quad (8)$$

Herein, \mathcal{R} denotes the ideal gas constant, T the temperature, and the dimensionless parameter β_s is defined as surfactant elasticity, which measures the sensitivity of the interfacial tension to the surfactant concentration. This equation describes the fact that the interfacial tension drops steeply as the surfactant concentration approaches unity from below [Chang and Franses, 1995]. However, this relation could predict unrealistic behaviours namely that the interfacial tension becomes negative for finite value of Γ . To avoid this, the relation is modified as follows:

$$\sigma/\sigma_s = \max \left[0.05, 1 + \beta_s \ln \left(1 - \frac{\Gamma}{\Gamma_\infty} \right) \right]. \quad (9)$$

density, ρ , and the viscosity, μ , are given by:

$$\begin{aligned} \rho(\mathbf{x}, t) &= \rho_o + (\rho_w - \rho_o) \mathbf{H}(\mathbf{x}, t), \\ \mu(\mathbf{x}, t) &= \mu_o + (\mu_w - \mu_o) \mathbf{H}(\mathbf{x}, t), \end{aligned}$$

where $\mathbf{H}(\mathbf{x}, t)$ represents a numerical Heaviside function, which is zero in the oil phase and unity in the water phase. The subscripts are used to indicate the corresponding liquid phases such that w is for water and o refers to oil. In Eq. (2), C_s is the Smagorinsky-Lilly coefficient, which is fixed to the value 0.2 as it varies between 0.1-0.3 in the literature [Lilly, 1966, 1967, Deardorff, 1970, McMillan and Ferziger, 1979, Pope, 2004]. Next, Δ is equivalent to $V^{1/3}$ where V is the volume of a grid cell, $V = \Delta x \Delta y \Delta z$ and $|\bar{S}| = \sqrt{2 \bar{S}_{ij} \bar{S}_{ij}}$ with \bar{S}_{ij} being the strain rate tensor [Pope, 2004, Meyers and Sagaut, 2006]. The term \mathbf{F}_{fsi} denotes the solid-fluid interaction force, and the last term on the right-hand-side in Eq. (2) accounts for the local interfacial force, which is decomposed into its normal component, $\sigma \kappa \mathbf{n}$, associated to the mean interface tension, and its tangential component, $\nabla_s \sigma$, the Marangoni stress; here, κ is twice the mean interface curvature, ∇_s is the surface gradient operator (i.e., $\nabla - \mathbf{n}(\mathbf{n} \cdot \nabla)$), \mathbf{n} is the outward-pointing unit normal to the interface, and A_e is the normalised area of a triangular Lagrangian mesh element, e . Finally, \mathbf{x}_f is a parameterization of the interface, and $\delta_f(\mathbf{x} - \mathbf{x}_f)$ is a Dirac distribution that is non-zero only when $\mathbf{x} = \mathbf{x}_f$.

In the present work, surfactant is soluble in the bulk (the continuous phase), such that surfactant transport is resolved both in the bulk and on the interface. The interfacial concentration, Γ , is governed by:

$$\frac{\partial \Gamma}{\partial t} + \nabla_s \cdot (\Gamma \mathbf{u}_t) = D_s \nabla_s^2 \Gamma + J. \quad (3)$$

More specifically, the left-hand-side terms represent the transient transport and the convection caused by the bulk flow,

206 The governing equations are recast in dimensionless form
 207 according to the following scaling:

$$\begin{aligned}\tilde{\mathbf{x}} &= \frac{\mathbf{x}}{D}, & \tilde{t} &= \frac{t}{1/N}, & \tilde{\mathbf{u}} &= \frac{\mathbf{u}}{ND}, & \tilde{\mathbf{g}} &= \frac{\mathbf{g}}{g}, \\ \tilde{p} &= \frac{\bar{p}}{\rho_w(ND)^2}, & \tilde{\mu} &= \frac{\mu}{\mu_w}, & \tilde{\rho} &= \frac{\rho}{\rho_w}, \\ \tilde{\sigma} &= \frac{\sigma}{\sigma_s}, & \tilde{\Gamma} &= \frac{\Gamma}{\Gamma_\infty}, & \tilde{C} &= \frac{C}{C_0}, & \tilde{C}_{\text{sub}} &= \frac{C_{\text{sub}}}{C_0},\end{aligned}\quad (10)$$

208 where the tildes indicate the dimensionless quantities. Here,
 209 space \mathbf{x} and time t are made non-dimensional by the im-
 210 peller diameter, D , and the duration for one impeller rota-
 211 tion revolution, $1/N$, respectively. Hence, the velocity and
 212 pressure are scaled using the impeller velocity, ND , and
 213 $\rho_w(ND)^2$, respectively. Moreover, C_0 denotes the initial
 214 surfactant concentration in the bulk. On this basis, the gov-
 215 erning equations become:

$$\nabla \cdot \tilde{\mathbf{u}} = 0, \quad (11)$$

$$\begin{aligned}\tilde{\rho} \left(\frac{\partial \tilde{\mathbf{u}}}{\partial \tilde{t}} + \tilde{\mathbf{u}} \cdot \nabla \tilde{\mathbf{u}} \right) + \nabla \tilde{p} &= \frac{1}{\text{Re}} \nabla \cdot \tilde{\mu} (\nabla \tilde{\mathbf{u}} + \nabla \tilde{\mathbf{u}}^T) \\ - \nabla \cdot (\tilde{\rho} 2C_s^2 \tilde{\Delta}^2 |\tilde{S}|) (\nabla \tilde{\mathbf{u}} + \nabla \tilde{\mathbf{u}}^T) &+ \frac{1}{\text{Fr}} \tilde{\rho} \tilde{\mathbf{g}} + \tilde{\mathbf{F}}_{\text{fsi}} \\ + \frac{1}{\text{We}} \left(\int_{\tilde{A}_e} (\tilde{\sigma} \tilde{\mathbf{n}} + \nabla_s \tilde{\sigma}) \delta_f(\tilde{\mathbf{x}} - \tilde{\mathbf{x}}_f) d\tilde{A}_e \right).\end{aligned}\quad (12)$$

$$\frac{\partial \tilde{\Gamma}}{\partial \tilde{t}} + \nabla_s \cdot (\tilde{\Gamma} \tilde{\mathbf{u}}_t) = \frac{1}{\text{Pe}_s} \nabla_s^2 \tilde{\Gamma} + \tilde{J}, \quad (13)$$

$$\tilde{J}_{a/d} = \text{Bi} [k \tilde{C}_{\text{sub}} (1 - \tilde{\Gamma}) - \tilde{\Gamma}], \quad (14)$$

$$\tilde{J}_{\text{diff}} = -\frac{1}{\text{Pe}_b h} \mathbf{n} \cdot \nabla \tilde{C}|_{\text{sub}} \quad (15)$$

$$\frac{\partial \tilde{C}}{\partial \tilde{t}} + \tilde{\mathbf{u}} \cdot \nabla \tilde{C} = \frac{1}{\text{Pe}_b} \nabla^2 \tilde{C}, \quad (16)$$

$$\tilde{\sigma} = \max [0.05, 1 + \beta_s \ln (1 - \tilde{\Gamma})]. \quad (17)$$

218 In these equations, the dimensionless parameters are de-
 219 fined as follows:

$$\begin{aligned}\text{Re} &= \frac{\rho_w ND^2}{\mu_w}, & \text{Fr} &= \frac{N^2 D}{g}, & \text{We} &= \frac{\rho_w N^2 D^3}{\sigma_s}, \\ \text{Pe}_b &= \frac{ND^2}{D_b}, & \text{Pe}_s &= \frac{ND^2}{D_s}, & \text{Bi} &= \frac{k_d}{N}, \\ h &= \frac{\Gamma_\infty}{DC_0}, & k &= \frac{k_a C_0}{k_d}, & \beta_s &= \frac{RT\Gamma_\infty}{\sigma_s}.\end{aligned}\quad (18)$$

221 Re, Fr and We are the Reynolds number (ratio of inertial to
 222 viscous forces), Froude number (ratio of inertial to gravita-
 223 tional force) and Weber number (ratio of inertial forces to
 224 interfacial tension), respectively. Pe_b and Pe_s are the bulk
 225 and interfacial Peclét numbers, separately providing the rel-
 226 ative significance of convection and diffusion in the bulk and
 227 on the interface. The Biot number, Bi, expresses the ratio

of characteristic desorptive to convective speed on the inter-
 face; h stands for the adsorption depth that characterises the
 diluted region beneath the interface caused by adsorption;
 k is the adsorption parameter, which represents the ratio of
 adsorption coefficient, k_a , to desorption coefficient, k_d . All
 these parameters are well known in literature [Batchvarov
 et al., 2020, 2021, Constante-Amores et al., 2020, 2021a,b,
 2023]. For simplicity, the tildes that designate dimension-
 less quantities are dropped henceforth. Finally, the dimen-
 sionless timescale we use in the following discussion, in the
 form of $t = n \times \text{Rev.}$, refers to the instant when n impeller
 revolutions are completed.

To achieve high-fidelity simulation regarding the dynamic
 interface and its interfacial tension forces, we use a hybrid
 front tracking/level-set technique, which is known as the Level
 Contour Reconstruction Method (LCRM) [Shin et al., 2018],
 where the surfactant transport and interfacial stresses shown
 above are well-resolved. Adaptive time steps are applied
 in our temporal discretisation process, which is based on
 second-order GEAR method, and the time-step value Δt is
 carefully chosen at each temporal iteration in order to satisfy
 a robust numerical stability via a criterion based on:

$$\Delta t \leq \min \{ \Delta t_{\text{cap}}, \Delta t_{\text{vis}}, \Delta t_{\text{CFL}}, \Delta t_{\text{int}}, \Delta t_{\text{surf}} \} \quad (19)$$

where Δt_{cap} , Δt_{vis} , Δt_{CFL} , Δt_{int} , and Δt_{surf} represent the
 capillary, viscous, Courant-Friedrichs-Lewy (CFL), interfacial
 CFL, and surfactant time-steps, respectively, defined by:

$$\Delta t_{\text{cap}} \equiv \frac{1}{2} \left(\frac{(\rho_o + \rho_w) \Delta x_{\text{min}}^3}{\pi \sigma} \right)^{1/2},$$

$$\Delta t_{\text{vis}} \equiv \min \left(\frac{\rho_w}{\mu_w}, \frac{\rho_o}{\mu_o} \right) \frac{\Delta x_{\text{min}}^2}{6},$$

$$\Delta t_{\text{CFL}} \equiv \min \left(\min_{\text{domain}} \left(\frac{\Delta x_j}{\|u_j\|} \right) \right),$$

$$\Delta t_{\text{int}} \equiv \min \left(\min_j \left(\frac{\Delta x_j}{\|U\|} \right) \right),$$

$$\Delta t_{\text{surf}} \equiv \frac{\Delta x_{\text{min}}^2}{6D_b},$$

where $\Delta x_{\text{min}} = \min_j(\Delta x_j)$ refers to the minimum size x at a
 given cell j ; u_j , and U are the maximum fluid and interface
 velocities, respectively.

In addition, the Direct Forcing Method used by Mohd-
 Yusof [1997] and Fadlun et al. [2000] is applied to incor-
 porate the complex geometry of the impeller and its rota-
 tion. More information on the numerical technique applied
 to computation and related validations can be found in [Rus-
 sell et al., 2019, Kahouadji et al., 2022, Liang et al., 2022].

2.3. Parameter values adopted in simulations

In our previous work [Liang et al., 2022], we investigated
 the interface evolution under a range of impeller speeds ($f =$
 $1 - 10$ Hz, $\text{Re} = 1802 - 18026$). Herein, we fixed the im-
 peller speed to $f = 5$ Hz, since our concern is currently
 on the effect of surfactant. This gives values of $\text{Re} = 9013$,

We= 55, and Fr= 0.1. The large Weber number which characterises our flow indicates the heavy dominance of inertial forces in the system; in addition, as we present in the next section, complex interacting structures (or vortices) are generated (see Figure 2). Hence, the studied system, especially the region near the impeller, is treated as turbulent, where the physics we extract is therefore generic to turbulent oil-water emulsification in stirred vessels.

To investigate the surfactant effect, we set up a “base” surfactant-laden case with surfactant-related parameters fixed to $C_0 = 4 \times 10^{-4} \text{ mol m}^{-3}$, $k_a = 6.68 \times 10^4 \text{ m}^3 \text{ mol}^{-1} \text{ s}^{-1}$, $k_d = 3.14 \text{ s}^{-1}$, and $\Gamma_\infty = 1 \times 10^{-5} \text{ mol m}^{-2}$. In particular, C_0 is calculated via $C_0 = \Gamma_\infty / R$, where R is the radius of the impeller, as a reference bulk concentration, which is also chosen as its initial value. Typical values for the surfactant adsorption and desorption coefficients, k_a and k_d , are quoted from relevant reviews provided in [Pan et al., 1998, Dong et al., 2000, He et al., 2015], where k_d is claimed to be within the range of $O(10^{-4}) < k_d [\text{s}^{-1}] < O(10^2)$ depending on the chemical structure of the surfactant molecules, while k_a is in the range $O(10^{-1}) < k_a [\text{m}^3 \text{ mol}^{-1} \text{ s}^{-1}] < O(10^6)$. In our base case, k_a and k_d are selected as the listed values exploring the scenario where the surfactant is inclined to absorb onto the interface, with a ratio of adsorption to desorption $k = k_a C_0 / k_d \approx 10$. In this limit, combined with the value of Bi determined via $k_d / N (= O(10^{-1})$ indicating a fast convection driven by ambient flow in comparison to surfactant desorption), the adsorbed surfactant can approximately perform as an insoluble layer. In addition, the maximum packing concentration at the interface is set to $\Gamma_\infty \approx O(10^{-5}) \text{ mol m}^{-2}$, as the same order of magnitude reported in experimental results for the surfactant such as Sodium Dodecyl Sulphate (SDS) [Chang and Franses, 1995, Levchenko et al., 2002]. This gives the values of $\beta_s \approx 0.7$ computed using the room temperature, $T = 298.15 \text{ K}$, and $h \approx 0.5$. An upper and lower limit of β_s , in addition to the base case, are investigated to recover the effect of surfactant sensitivity (i.e., $\beta_s = 0.5, 0.7, 0.9$).

We also fix both Peclet numbers in the bulk and on the interface as $Pe_b = Pe_s = 4.6 \times 10^2$. This comes from the recent remarks from Constante-Amores et al. [2021a,b] and Kamat et al. [2018] stating that negligible effect arises from Pe_s when it is increased further above 10^2 ; moreover, Pe_b is kept equal to Pe_s as suggested in Constante-Amores et al. [2021a], which also follows the guideline given by Ratulowski and Chang [1990] to achieve a balance between adsorption and interfacial convection, assuring both convective and diffusive transport are resolved in the simulated system.

Finally, as mentioned previously, a second effect from surfactant arises from the Marangoni stress, which is induced due to the surfactant concentration gradient and hence can be computed via Γ :

$$\tau \equiv \nabla_s \sigma \cdot \mathbf{t} = -\frac{\beta_s}{1 - \Gamma} (\mathbf{t} \cdot \nabla_s \Gamma). \quad (20)$$

To isolate this effect from that induced by the interfacial tension reduction, another surfactant-laden case is set up where

the Marangoni stress is turned off by eliminating the term $\nabla_s \sigma$ from Eq. (2). This additional case allows us to unequivocally elucidate the mechanisms by which the interfacial tension reduction and surfactant concentration gradient conspire to modify the surfactant-free interface dynamics.

3. Results and Discussion

In this section, we present a discussion of our results, starting with a comparison of the current predictions against our previous work where we studied the flow profiles and interfacial dynamics inside a surfactant-free agitated vessel (of identical configurations) [Liang et al., 2022]. Using qualitative visualisation and quantitative statistics (i.e., time evolution of dispersed entity number and drop size distribution at the instant where the simulation is terminated), the comparison provides an insight into how the presence of surfactant modifies the liquid dispersion process in the studied system. We then demonstrate the effect of surfactant elasticity (β_s) via a parametric study.

3.1. Surfactant-free system from previous work

Prior to the discussion of the roles played by the surfactant, the flow field generated in the current configuration, and surfactant-free interface evolution are briefly considered. Generally, as presented in Figure 2, the impeller pumps the flow radially outward (analogous to the von Kármán flow over a infinite rotating disc [Schlichting and Kestin, 1961]). The no-slip fixed vessel wall modifies this flow, along which the flow develops upward to the interface. After this, the flow is dragged to the vessel center by a centrifugal force at the interface. Finally, a strong elongational flow is presented in the vessel center, which indicates a large tendency for the fluid to travel down back to the impeller, giving rise to flow circulation. Such a process generates a myriad of vortical structures and therefore a flow field of high complexity where different mechanisms govern the drop deformation depending on the local flow type [Paul et al., 2004].

Following the flow field described, the liquid dispersion in the studied configuration is achieved by following several steps: (1) *interface deformation*: the rotating impeller deforms the flat interface downward in a swirling motion until both contact; (2) *ligament formation*: the impeller shear cuts off the deforming interface giving birth to ligament(s); (3) *drop breakup*: the ligament elongates until it breaks into multiple individual drops via a capillary instability (see Figure 6, and detailed mechanism has been described in [Janssen and Meijer, 1993] as “transient dispersion” or “capillary breakup”). Likewise, this breakup mechanism is analogous to the “end-pinch” phenomenon described in Janssen et al. [1994], which refers to the breakup of an elongated drop after a sudden halt of the flow rate, where the flow rate interruption corresponds to the inherently periodic velocity field [Wu and Patterson, 1989, Li et al., 2017, Fan et al., 2021] introduced by the impeller rotation herein. Particularly for the current impeller speed, there exists a retraction of the deforming interface (due to the interfacial tension competing against the

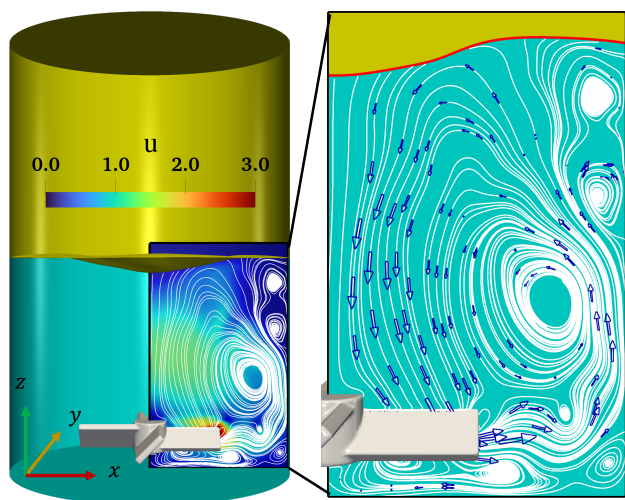


Figure 2: Flow field prior to the interface deformation ($t = 8 \times Rev.$) for a surfactant-free system, represented by streamlines drawn on a $x - z$ plane at $y = 4.3\text{cm}$. The inset of the three-dimensional vessel is coloured by the velocity magnitude, and the blue arrows shown in the close-up view (representing velocity orientations) are scaled by the velocity magnitude.

374 elongational flow), which leads to (4) *the cessation of interface-*
 375 *impeller contact* and no further ligaments being produced.
 376 Meanwhile, the dispersed entities are likely to travel up to
 377 the overlying oil phase given the underlying flow field, and
 378 in addition, due to buoyancy.

379 3.2. Surfactant effect on interface evolution

380 In this part, we compare three cases with regard to the
 381 interface evolution described above including (1) surfactant-
 382 free system from our previous work, (2) surfactant-laden I
 383 ($|\tau| > 0$), and (3) surfactant-laden II with Marangoni stress
 384 turned off ($|\tau| = 0$).

385 3.2.1. Step 1: Interface deformation

386 Figure 3 presents the interfacial shapes at early times
 387 ($t = 8.5 - 12 \times Rev.$) for the three cases, where the interface
 388 begins to deviate from its flat position, and a few dispersed
 389 entities are formed. The first observation that can be drawn
 390 from the figure is that the deformation of the surfactant-laden
 391 interface (I) is accelerated in comparison to its surfactant-
 392 free counterpart (see Figure 3-(a) – (b) and -(f) – (g)). This
 393 is expected since the presence of surfactant reduces the aver-
 394 age interfacial tension, and therefore, promotes the inter-
 395 face deformation under the same flow condition. However,
 396 Figure 3-(c) and -(h) show that the deforming interfaces for
 397 the two cases subsequently reach similar positions (relative
 398 height in the vessel).

399 To better illuminate the observation, Figure 4-(a) depicts
 400 the deformation by plotting the temporal evolution, in terms
 401 of the minimum position of the interface and the correspond-
 402 ing axial component of interfacial velocity at that location
 403 (as schematically shown in Figure 3-(a)). The position refers
 404 to the relative height in the cylindrical vessel which is scaled
 405 using the height of vessel, $\tilde{z} = (2z - H)/H$, and only the

406 magnitude of velocity is plotted as $|u_z|$, since it always points
 407 downward during this step. This plot shows that while the in-
 408 terface approaches the impeller (decreasing \tilde{z}), $|u_z|$ increases
 409 to a peak value and then a reduction is seen. A similar con-
 410 clusion as above, that the accelerated deformation is asso-
 411 ciated with the surfactant-laden interface (I), can be made
 412 prior to the velocity peak. It is also evident that the subse-
 413 quent decrease in $|u_z|$ is more significant for the surfactant-
 414 laden case I. This can be explained by the fact that surfactant
 415 on the deforming interface is accumulated at its minimum
 416 position (i.e., the descending leading edge of the interface),
 417 which introduces an opposing Marangoni stress pointing up-
 418 ward. Figure 4-(b) exemplifies the surfactant distribution
 419 on the interface at $t = 9 \times Rev.$. As shown, the induced
 420 Marangoni stress, which opposes the downward flow at the
 421 vessel center, acts to decelerate the interface deformation. A
 422 possible explanation to the overall acceleration prior to the
 423 velocity peak can be the dominance of the inertia, namely
 424 the strong downward flow where the retraction driven by
 425 the Marangoni stress is negligible. After that, the interface
 426 reaches the vicinity of the impeller, at which the flow field
 427 starts to develop radially, and therefore, the vertical defor-
 428 mation of interface slows down. Thus, the retarding effect
 429 of the Marangoni stress [Eggleton et al., 2001, Kamat et al.,
 430 2018] commences to function, causing the further decrease
 431 in $|u_z|$ seen for the surfactant-laden case I. This process of
 432 deformation is clearly described via \tilde{z} in Figure 4-(a) that,
 433 at $t = 10 \times Rev.$, the surfactant-laden interface (I) reaches
 434 the same height in the vessel as the surfactant-free interface
 435 after the acceleration and the subsequent deceleration.

436 Moreover, the effect of Marangoni stress demonstrated
 437 above can be better appreciated via the surfactant-laden sys-
 438 tem II. The visualisation of the Marangoni-free interface in-
 439 dicates that Marangoni stress plays a role in retaining the
 440 plump and thick shape of the deforming interface, as well as
 441 the relatively uniform surfactant concentration over the inter-
 442 face. The evidence can be seen in Figure 3-(k), which indi-
 443 cates that the Marangoni-free interface is in a slender shape
 444 with varying interfacial surfactant concentration, as opposed
 445 to what is shown for the surfactant-laden system in the pres-
 446 ence of Marangoni stress. Additionally, from Figure 4-(a),
 447 decelerating deformation occurs for the Marangoni-free sys-
 448 tem while the interface is near the impeller. However, the
 449 “braking” (i.e., $|u_z| \rightarrow 0$ and the negligible change in \tilde{z}) ob-
 450 served for the other two cases no longer takes place, which
 451 provides additional support to the previous statement that
 452 Marangoni stress leads to further deceleration of interface
 453 deformation in addition to that which arises due to the radially-
 454 developing flow field.

455 Another interesting phenomenon is the formation of the
 456 “branches” at the surfactant-laden interface (I) (see Figure 3-
 457 (i)). Such phenomenon can be related to the fact that given
 458 the underlying flow described above, where the flow devel-
 459 ops toward the vessel wall, ligaments are prone to be formed
 460 elongating radially behind the impeller hub. Furthermore,
 461 this can be better demonstrated using the flow topology pa-
 462 rameter, Q , which was first used in Perry and Chong [1987]

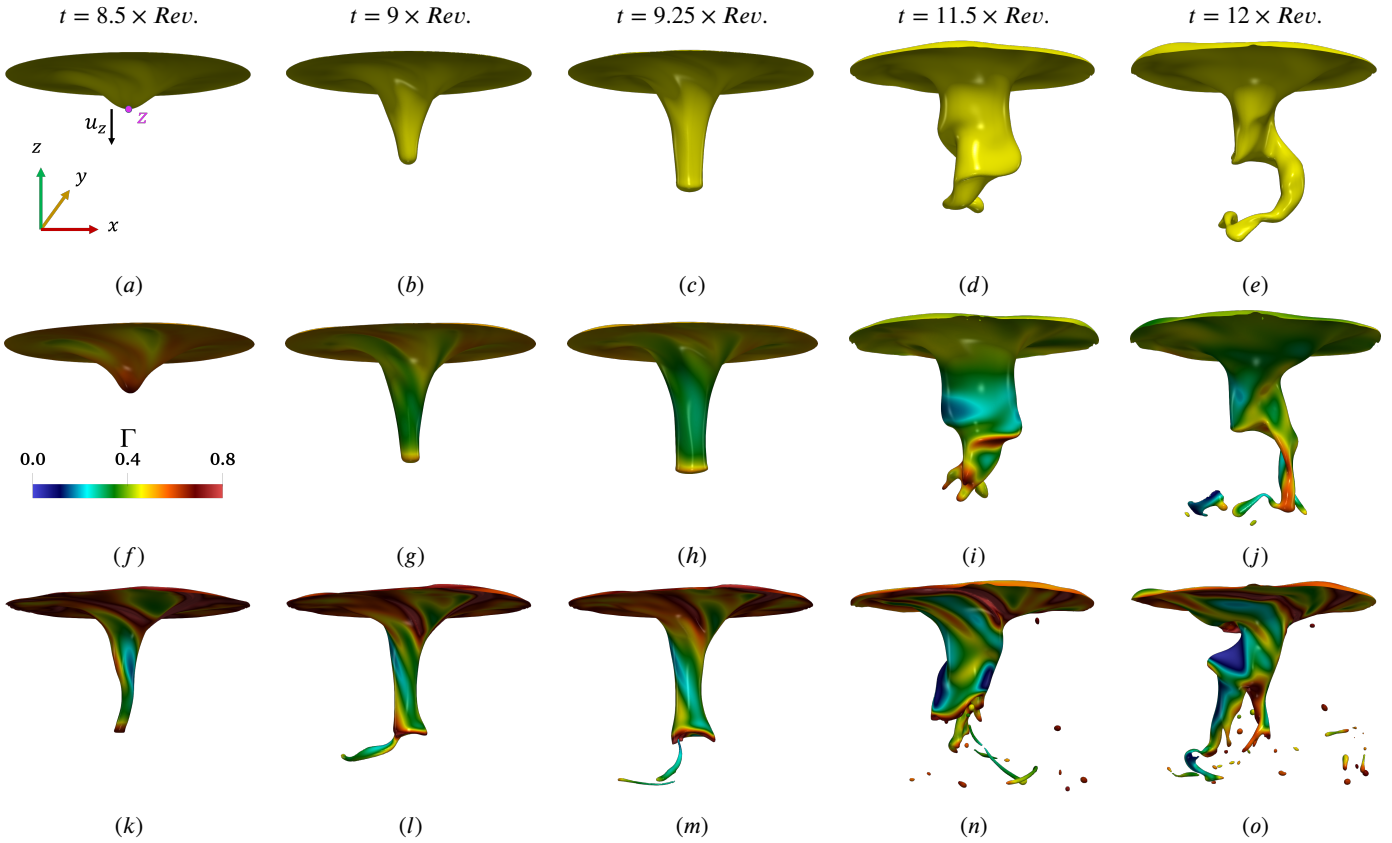


Figure 3: Comparative evolution of interfacial shapes for the surfactant-free (top), surfactant-laden I ($|\tau| > 0$, middle) and surfactant-laden II ($|\tau| = 0$, bottom) systems for $t = 8.5 - 12 \times Rev.$. The interface is coloured by the magnitude of Γ . The values of surfactant-related parameters correspond to the “base” case (see Section 2.3).

463 and recently became popular in the field of multiphase flows
 464 [Soligo et al., 2020b]. This parameter helps distinguish among
 465 the three types of flow topology locally and is computed using
 466 the rate-of-deformation, \mathbf{D} , and rate-of-rotation tensors,
 467 $\mathbf{\Omega}$:

$$Q = \frac{\mathbf{D}^2 - \mathbf{\Omega}^2}{\mathbf{D}^2 + \mathbf{\Omega}^2} \begin{cases} = -1, & \text{for rotational flow} \\ = 0, & \text{for shear flow} \\ = +1, & \text{for elongational flow,} \end{cases} \quad (21)$$

where $\mathbf{D}^2 = \mathbf{D} : \mathbf{D}$ and $\mathbf{\Omega}^2 = \mathbf{\Omega} : \mathbf{\Omega}$; \mathbf{D} and $\mathbf{\Omega}$ can be calculated from the velocity gradient tensor $\nabla \mathbf{u}$:

$$\mathbf{D} = \frac{\nabla \mathbf{u} + \nabla \mathbf{u}^T}{2},$$

$$\mathbf{\Omega} = \frac{\nabla \mathbf{u} - \nabla \mathbf{u}^T}{2}.$$

468 Figure 5 compares the probability density function (P.D.F.)
 469 of parameter Q at the surfactant-free and surfactant-laden
 470 interfaces (I) at $t = 11.5 \times Rev.$, corresponding to Fig-
 471 ure 3-(d) and -(i), respectively. In this case, the statistics
 472 are only computed at the interface, which excludes the effect
 473 of internal and external flow enabling us to isolate the flow
 474 modification induced by the interfacial tension reduction.
 475 Nevertheless, albeit not presented herein, negligible differ-
 476 ence is observed in terms of the internal and external flow

types for both systems (dominated by the pure shear flows),
 which indicates that the flow modification is mainly at the
 interface. As can be seen from Figure 5, for a surfactant-
 covered interface (I), there is a decreasing possibility of see-
 ing elongation-dominated flow, while a larger probability to
 experience shear-like flow is observed. This could be a pos-
 sible explanation for “branch” formation as the deforming
 interface is more likely to be torn apart, rather than being
 stretched, under the modified flow topology. Consequently,
 these “branches” give way to ligament development accom-
 panied by dispersed drop production via a surfactant-induced
 tip-streaming mechanism (more discussion in the following
 Section 3.2.2). In contrast, as shown in Figure 3-(e), the
 surfactant-free interface keeps elongating and thinning,
 following a helical trajectory due to the impeller rotation,
 until the first ligament is formed ($\approx 12.375 \times Rev.$, which is not
 presented in the figure).

For the Marangoni-free system, a sequence of thin ligan-
 tments are produced at the minimum position of the inter-
 face (Figure 3-(l), (m)), quickly followed by the formation
 of highly surfactant-concentrated drops (Figure 3-(n), (o)),
 all of which is a consequence of the plummeting interfacial
 tension that takes place in regions with surfactant sur-
 plus. These observations, once again, reflect the fact that
 Marangoni stress is activated to avoid surfactant from accu-

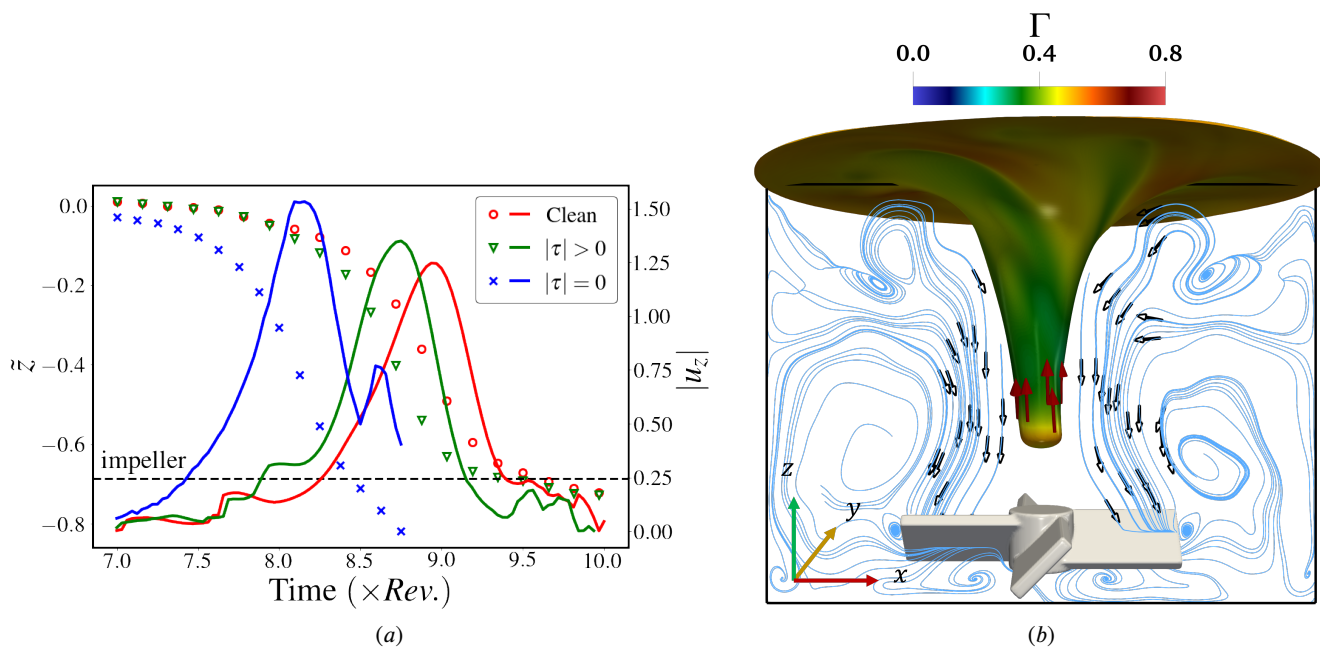


Figure 4: (a) Temporal evolution of the interfacial deformation for the three studied cases for $t = 7 - 10 \times Rev.$ with regard to the minimum position of the deforming interface (\bar{z} shown by symbols) and the magnitude of the velocity of the vertical interface deformation ($|u_z|$ shown by lines); (b) the interplay between the flow field (streamlines in blue along with black arrows representing their directions) at the vessel center and the induced Marangoni stresses (red arrows) at the deforming interface for $t = 9 \times Rev.$. The interface is coloured by the magnitude of Γ . The surfactant-related parameter values remain unchanged from Figure 3.

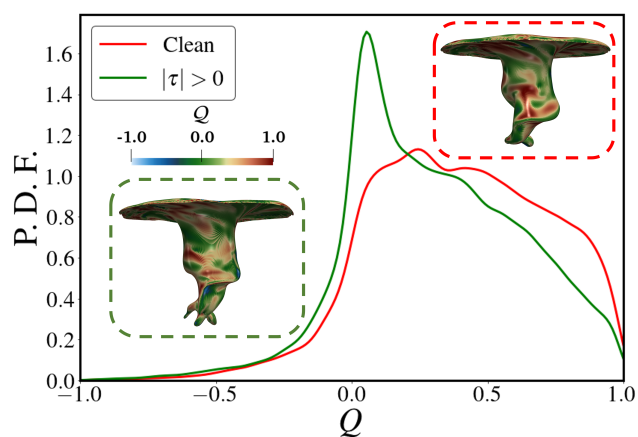


Figure 5: Probability density function of parameter Q for surfactant-free and surfactant-laden I interfaces at $t = 11.5 \times Rev.$. The interfaces are coloured by Q . The surfactant-related parameters are the same as in Figure 3.

502 mulating in excess at the minimum position of the interface.
 503 The absence of this phenomenon is directly responsible for
 504 the “free” escape and detachment of ligaments from the
 505 deforming interface, as seen in Figure 3-(m), (n).

506 3.2.2. Steps 2&3: Ligament and drop formation

507 As indicated earlier, during Steps 2 and 3, a large amount
 508 of dispersed entities is produced via distinct mechanisms. In
 509 our previous work, we suggested that following the ligament
 510 generation, the dispersed drops in surfactant-free system are

511 formed via a capillary instability (see Figure 6), where one
 512 elongated ligament gives birth to multiple individual drops.
 513 For the surfactant-laden I system, an additional drop breakup
 514 mechanism is promoted, namely tip-streaming/dropping [Groeneweg
 515 et al., 1994, Eggleton et al., 2001]. Figure 6 displays
 516 the close-up visualisations of various drop breakup events
 517 observed in the surfactant-free and surfactant-laden I sys-
 518 tems (during $t = 12 - 18 \times Rev.$), exemplifying those via
 519 capillary instability and tip-streaming. For the former mech-
 520 anism, two examples from different systems are presented,
 521 whereas two scenarios for surfactant-induced tip-streaming
 522 are extracted from the surfactant-laden I system. The first tip
 523 streaming is initiated from the deforming interface, which
 524 leads to an individual drop formation prior to long ligament
 525 formation, in contrast to what we observed from the surfactant-
 526 free system (see Section 3.1). This can be an influencing fac-
 527 tor on the transient dispersed entities number profile (more
 528 details are deferred to Section 3.3.1). Likewise, in the sec-
 529 ond case, where the breakup is from an elongated ligament,
 530 tip-streaming generates drops intermittently, leaving a large
 531 and relatively clean (i.e., covered by less surfactant) drop after
 532 emission of several daughter drops.

533 An interesting feature for the Marangoni-free case is that
 534 drop breakup via capillary instability is suppressed, and dis-
 535 persed drops are formed via either binary breakup from larger
 536 drops or tip-streaming from stretching ligaments. Figure 7-
 537 (a) illustrates the effect of Marangoni stresses on the stretch-
 538 ing ligament prior to its breakup via capillary instability (us-
 539 ing the example shown in Figure 6). As presented, Marangoni
 540 stresses play different roles on each end of the ligament de-

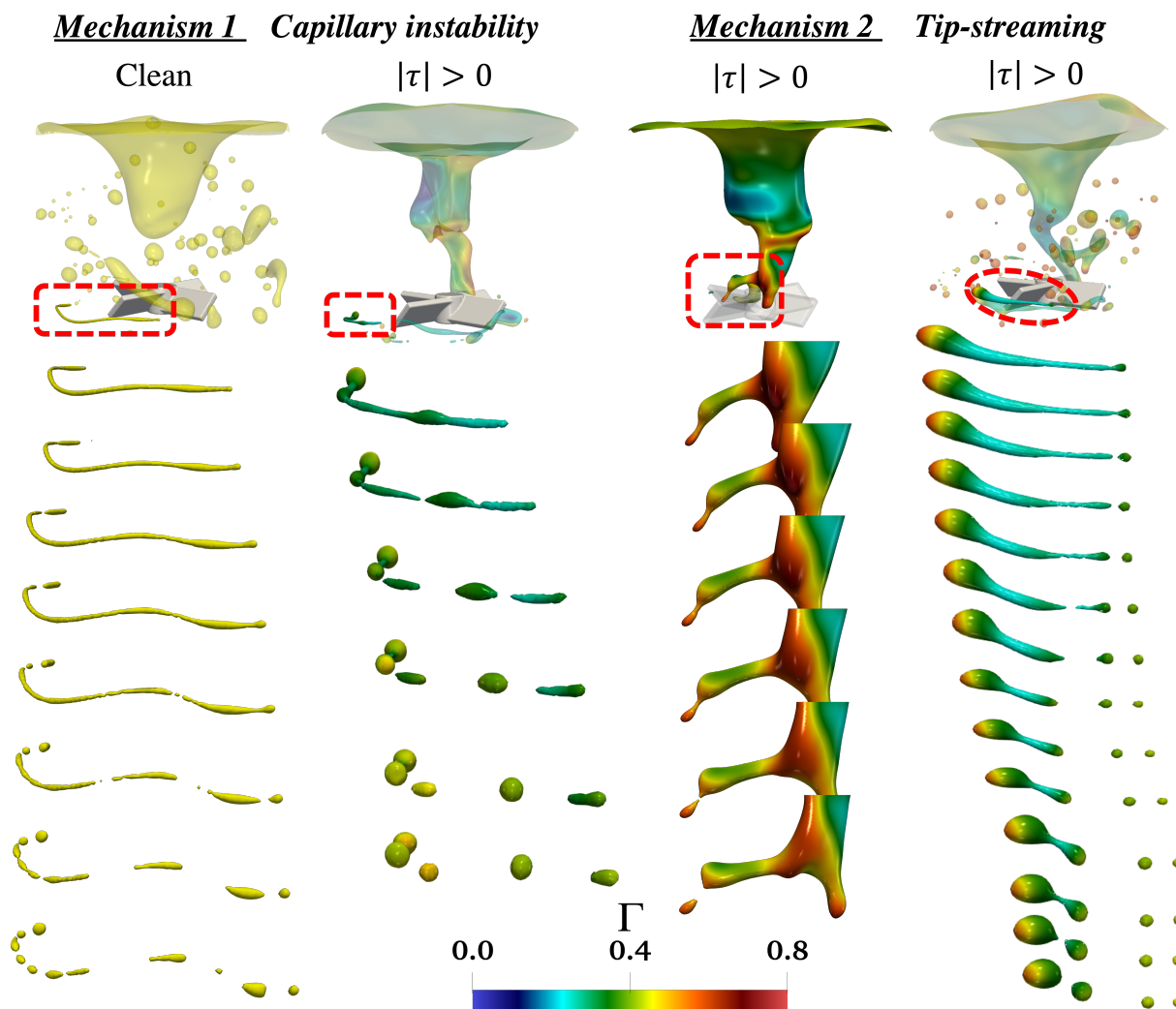


Figure 6: Close-up visualisations of drop breakup mechanisms observed in surfactant-free system (left) at $t = 16.375 \times Rev.$, and surfactant-laden I system, at $t = 11.625, 12.375, 15.4 \times Rev.$ (from second left to right, respectively). The presented breakup events are via the capillary instability (left two columns), and surfactant-enhanced tip-streaming (right two columns). Two scenarios for tip-streaming are given, one initiated from the deforming interface and another from an elongated ligament. The surfactant-related parameters remain unchanged from Figure 3.

541 pending on the local surfactant distribution. First, for the
 542 ligament pole labeled as *A*, surfactant is accumulated at the
 543 bulbous end, which introduces a Marangoni stress towards
 544 the ligament body, impeding the formation of an individ-
 545 ual drop. On the other hand, surfactant concentration at the
 546 pole *B* is lower relative to the nodule region, giving rise
 547 to a Marangoni stress pointing outward and thus enhancing
 548 the ligament elongation. From this perspective, Marangoni
 549 stress encourages the commencement of breakup events driven
 550 by capillary instability by facilitating the ligament's stretch-
 551 ing motion and inhibiting drops from bursting at the poles.
 552 This effect, combined with the promotion of tip-streaming,
 553 leads to the observation that both mechanisms exist in the
 554 surfactant-laden I system.

555 Nevertheless, in the case of drop deformation, it is com-
 556 mon to see the same surfactant distribution profile as in the

557 pole *A*, since surfactant tends to be swept towards the poles.
 558 As stated in the discussion related to Step 1, Marangoni stress
 559 acts as a stabilising factor against drop deformation, either
 560 delaying or even avoiding the new drop production in this
 561 step. Figure 7-(b) provides evidence of this by comparing the
 562 behaviour of one drop located in the vicinity of the impeller
 563 at $t = 15.5 \times Rev.$ for both surfactant-laden systems ($|\tau| = 0$
 564 and $|\tau| > 0$ shown at the top and bottom of the figure, re-
 565 spectively). The critical Weber number for drop breakup has
 566 been reported for various types of flows, which consistently
 567 lies in the range of $O(10^1)$, for instance, $We_{crit} \approx 1$ for tur-
 568 bulent emulsification [Hinze, 1955, Håkansson et al., 2022],
 569 $We_{crit} \approx 3 - 7$ in the cases of uniaxial shear and elongation
 570 flow [Grace, 1982] and nonuniform shear [Chin and Han,
 571 1980]. Based on this, both drops are likely to break given
 572 their sizes ($D_{d,|\tau|>0} = 0.53$ cm and $D_{d,|\tau|=0} = 0.40$ cm,

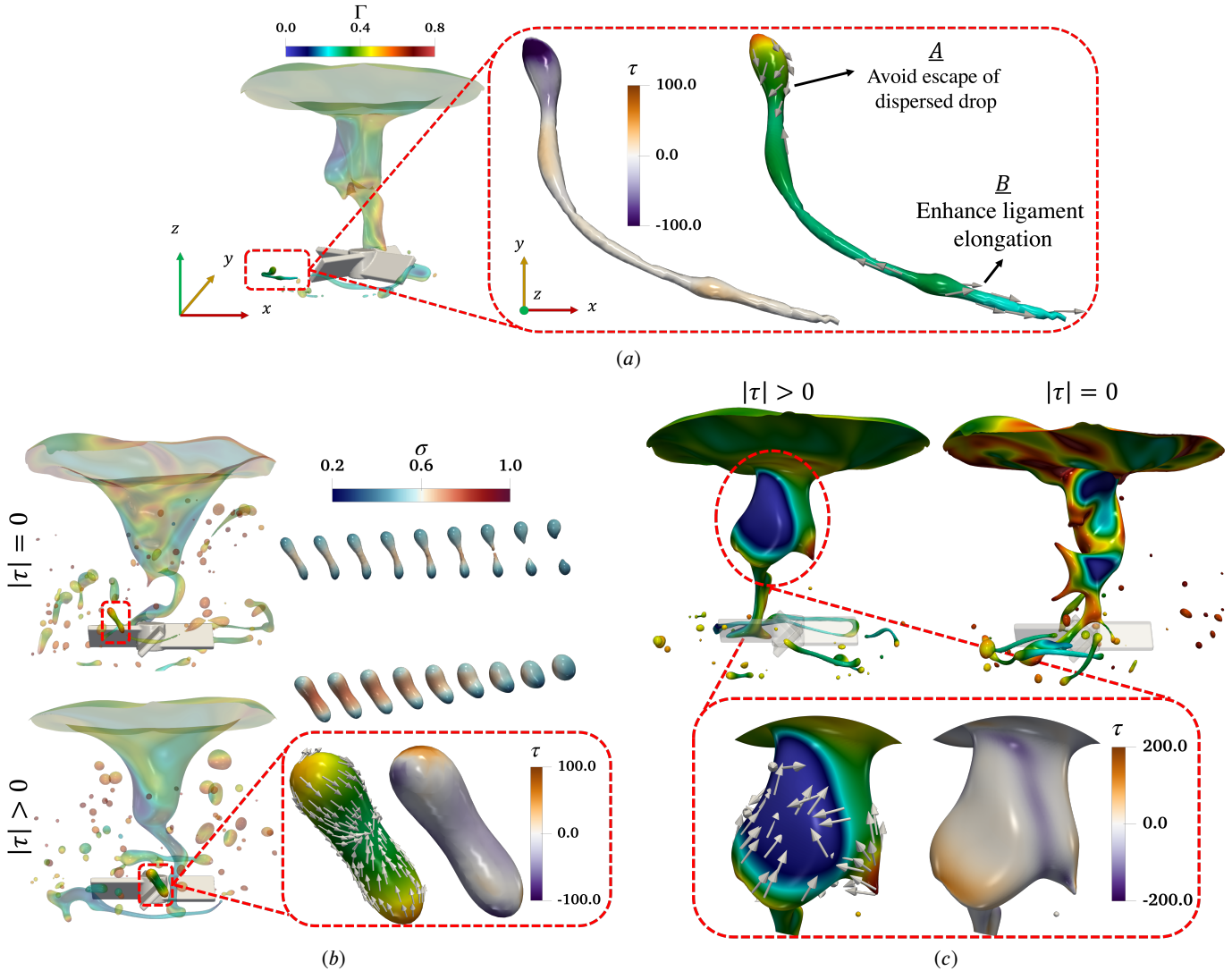


Figure 7: Visualisations of Marangoni stresses under different scenarios: (a) ligament elongation prior to its fragmentation towards multiple drops; (b) drop deformation where the evolving drops are coloured using σ ; and (c) evolution of the deforming interface shape. The insets consist of two identical interfacial states coloured in Γ and τ , respectively; the negative sign of τ represents its direction, and the grey arrows refers to the direction of Marangoni stresses. The surfactant-related parameters remain unchanged from Figure 3.

573 obtained as the corresponding sphere diameter of its interfacial area) and their local Weber numbers ($We_{|\tau|>0} = 103.6$
 574 and $We_{|\tau|=0} = 93.2$, calculated with the impeller tip velocity and average interfacial tension at the interface). How-
 575 ever, it is evident that the drop with Marangoni stress turned on retracts to its spherical shape rather than the predicted
 576 drop fragmentation according to We_{crit} . This is attributed to, as shown in the figure inset, the existence of Marangoni
 577 stress pointing from drop poles to drop equator. This comparison strengthens what has been demonstrated previously
 578 that Marangoni stress hinders elongation and induces the retraction of the drop back to its spherical shape. Furthermore,
 579 the presence of Marangoni stress reduces the deformability of the deforming interface making it more rigid as shown
 580 in Figure 7-(c). From the figure, surfactant is accumulated at the stretching tip of the deforming interface and is less
 581
 582
 583
 584
 585
 586
 587
 588

589 concentrated at the belly, which establishes a surfactant concentration gradient. Consequently, the induced Marangoni
 590 stress immobilises the interface preventing it from deforming into multiple branches (as shown for the Marangoni-free
 591 case), which is inclined to generate dispersed drops freely. 592
 593

3.2.3. Step 4: Cessation of interface-impeller contact

594 As mentioned previously, the deforming interface retracts
 595 upward at $t = 20 \times Rev.$, leading to the cessation of interface-
 596 impeller contact thereafter. Figure 8-(a) exemplifies the inter-
 597 facial behaviours for the three cases at $t = 25 \times Rev.$. As
 598 shown, the interface remains in a generally concave shape,
 599 which shows some resemblance to the well-known “New-
 600 ton’s Bucket” flow generated in a rotating cylinder [Laymon,
 601 1978, Jansson et al., 2006, Kahouadji and Witkowski, 2014],
 602 or the air-water surface deflection in the shape of an inverted
 603

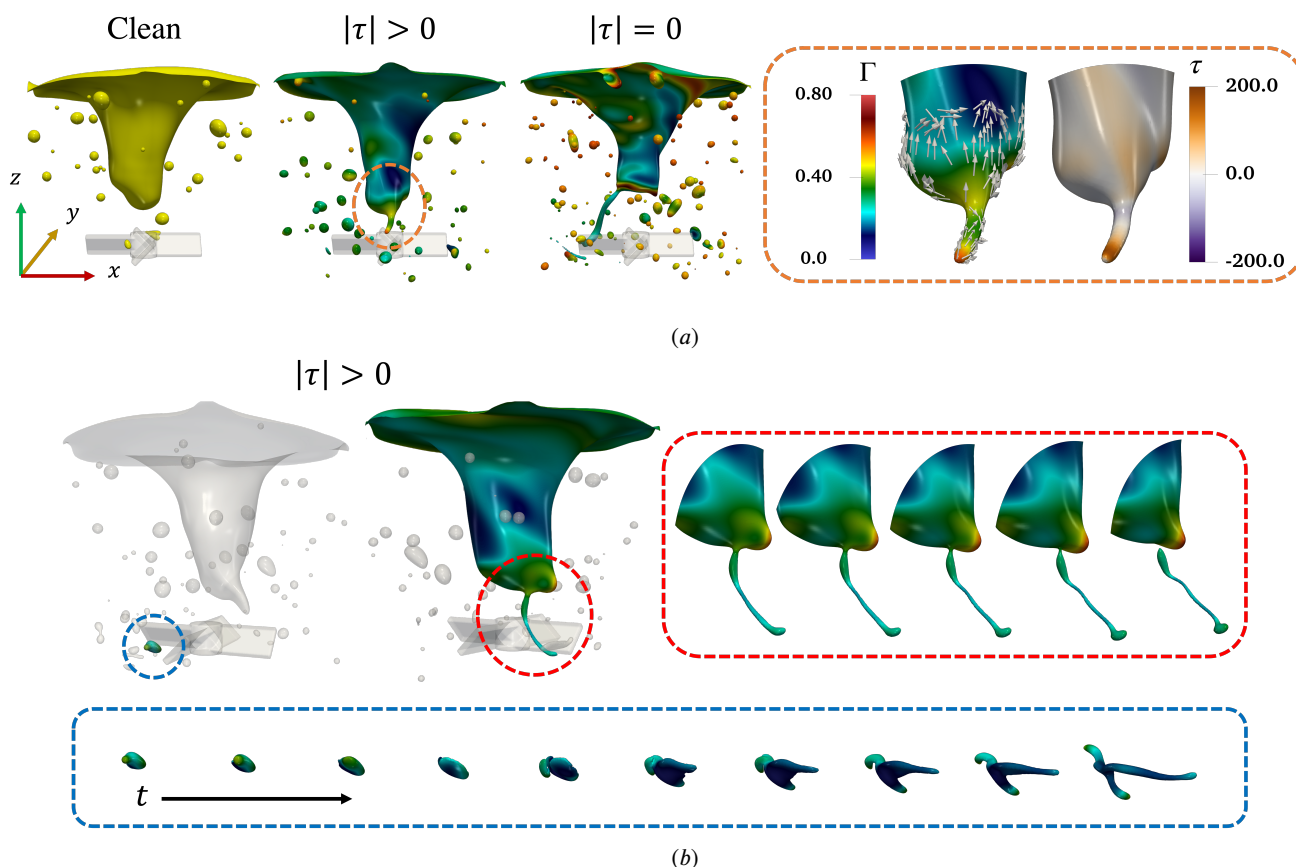


Figure 8: (a) Interfacial shapes for the three studied systems at $t = 25 \times Rev.$, along with a similar inset showing the direction and magnitude of Marangoni stress as in Figure 7; (b) exemplified interfacial evolution in the surfactant-laden I system presenting the different outcomes depending on dispersed drop behaviours. (i) Coalescence: ligament formation from consequent larger drop (circled in blue) elongation; (ii) merging back with the deforming interface: recurring ligament formation (circled in red) from the deforming interface. The surfactant-related parameters remain unchanged from Figure 3.

604 bell observed in rotating flows [Vatistas, 1990]. Herein, given
 605 the current impeller speed, the surfactant-free interface ro-
 606 tates following the impeller motion and no further ligaments
 607 are generated. In contrast, intermittent ligament forma-
 608 tion is seen for the two surfactant-laden systems despite the ces-
 609 sation of of interface-impeller contact. This is presumably
 610 caused by the surfactant accumulation at the minimum posi-
 611 tion of the interface which decreases the interfacial tension
 612 that would otherwise have counteracted ligament formation.
 613 In addition, the visualisation of interface in the presence of
 614 Marangoni stress highlights its increased rigidity (circled in
 615 orange in Figure 8-(a)) relative to its Marangoni-free coun-
 616 terpart, which indicates again the immobilising effect of the
 617 Marangoni stress against interfacial deformation.

618 It is also worth noting that the dispersed drop tends to
 619 either coalesce with one another or merge back with the “in-
 620 verted bell”. Each case leads to different outcomes, as exem-
 621 plified by the interfacial evolution in the case of surfactant-
 622 laden I system, as displayed in Figure 8-(b). In the first
 623 scenario, an emergent interfacial structure (circled in blue)
 624 formed from a coalescence event is elongated by the local
 625 flow and broken up again into several smaller drops. For
 626 the latter case, ligament production from the deforming in-

terface (circled in red) eventually recurs given that adequate
 dispersed drops are merged back with the deforming inter-
 face.

3.3. Comparative statistics

3.3.1. Temporal evolution of dispersed entity number

627 In this part, the transient count of dispersed entities is
 628 tracked with the aim of quantifying the qualitative interfacial
 629 behaviours described above. The four steps of liquid disper-
 630 sion (see Section 3.1) could be related to three stages
 631 of the transient number profile of dispersed entities (which
 632 can be either a stretching ligament or an individual drop).
 633 Figure 9-(a) presents the number profile along with the in-
 634 terfacial shape at the corresponding instants. Initially, *no*
 635 *dispersed drop* (Stage A, shown by dashed lines) forma-
 636 tion is observed during the interface deformation (Step 1) since
 637 the interface is approaching the impeller. Then, the onset of
 638 ligament formation and subsequent breakup events (Steps 2
 639 and 3) lead to a *dramatic increase* (Stage B, shown by solid
 640 lines) in the dispersed entity count. Finally, the cessation of
 641 impeller-interface contact (Step 4) gives rise to a *gentle fall-*
 642 *off* (Stage C, shown by dotted lines) as the dispersed drops
 643 tend to coalesce, or merge back with the overlying oil-phase
 644
 645
 646
 647
 648

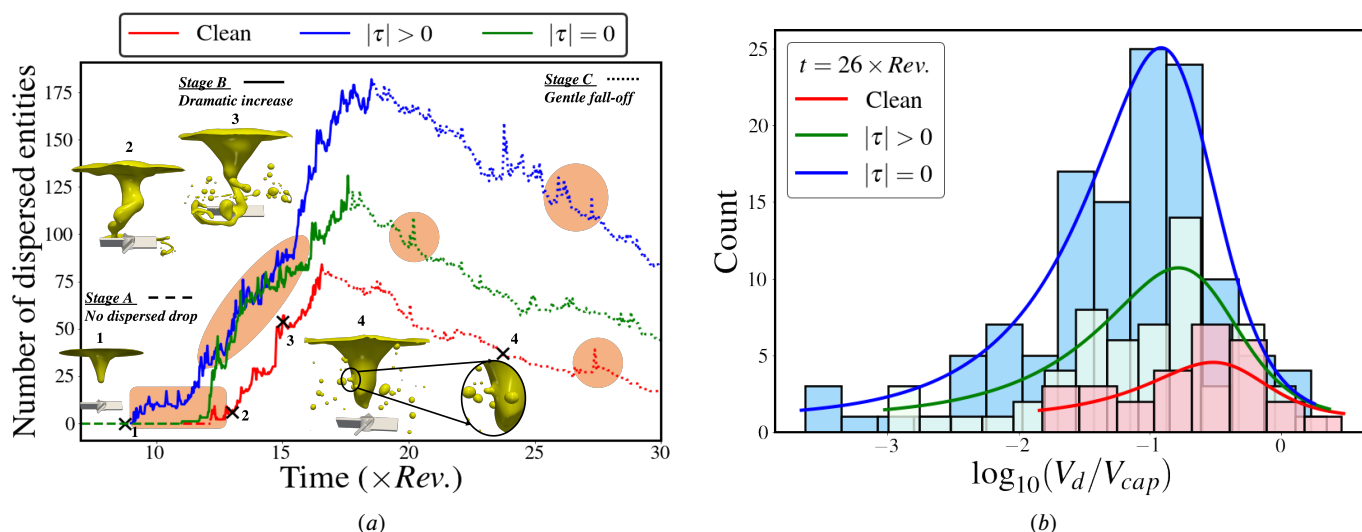


Figure 9: (a) Temporal evolution of dispersed entities number for surfactant-free, surfactant-laden I, and surfactant-laden II systems for a time frame of $t = 7 - 30 \times Rev.$, along with the representative interfacial shapes corresponding to the four steps of liquid dispersion (at $t = 9, 13, 15, 23.5 \times Rev.$, exemplified by the surfactant-free case). This profile is divided into three stages: (A) no dispersed drop, (B) dramatic increase and (C) gentle fall-off, which are respectively shown by dashed, solid, and dotted lines; (b) fitted drop size distribution (Probability Density Function with respect to log-scale of normalised drop volume) at $t = 26 \times Rev.$ for the three cases. The surfactant-related parameters remain unchanged from Figure 3.

649 (see close-up views in Figure 9-(a)), while less or no new
650 dispersed drops are formed.

651 The first distinction among the three cases is the compression
652 of Stage A corresponding to a shortened duration
653 of interface deformation. This can be explained with the accelerated
654 interface deformation as demonstrated above. Furthermore, we noted
655 here the distinguished increasing patterns at early Stage B for the three
656 cases, as highlighted in the orange rectangle in Figure 9-(a). The abrupt
657 jump seen for the surfactant-free system comes naturally from the
658 breakup events via the capillary instability. By comparison, a mild
659 increase appears prior to the steep rise for the surfactant-laden I
660 system, which is the result of the early drop breakup events via
661 tip-streaming from the deforming interface. Again, the early and more
662 pronounced increase for the Marangoni-free system reflects the
663 inhibiting effect of Marangoni stress on the drop deformation and
664 therefore the breakup events.

665 During Stage B in Figure 9-(a), an abrupt jump in the
666 number of dispersed entities with a larger amplitude compared to the
667 surfactant-free system is observed for the surfactant-laden I system
668 due to the onset of drop breakup events via both mechanisms stated
669 above (capillary instability, and concurrently, tip-streaming). However,
670 there exists a plateau following the dramatic increase ($t \approx 15 \times Rev.$),
671 which indicates a deceleration of the dispersed phases formation. This
672 can be related to the fact that tip-streaming, which generates drops
673 intermittently, is promoted in surfactant-laden I system, and
674 consequently, some ligaments generating drops via tip-streaming in
675 that system break up into drops via a capillary instability in
676 surfactant-free system. Another interesting trend is the overlap
677 between the two surfactant-laden cases, as highlighted in orange oval
678 in Figure 9-(a). As demon-
679
680

681 strated earlier, this reflects the fact that Marangoni stress aids
682 the commencement of breakup events via an capillary instability in
683 the system with Marangoni stress turned on, and thus dispersed drops
684 are generated rapidly enough to reach the comparable amount to its
685 counterpart for the Marangoni-free system, though a delayed appearance
686 of the first dispersed drop is observed for the former system. Following
687 the overlap, the drop count for the Marangoni-free system rises sharply
688 until its peak is reached. This is due to the fact that a large amount
689 of thin ligaments are formed simultaneously from the deforming
690 interface, along with the drop production, which give rise to similarly
691 increasing rate as in the case of a single breakup event via the
692 capillary instability. This provides additional evidence for the effect
693 of the Marangoni stress on the interfacial dynamics and associated
694 phenomena as reported in Section 3.2.2 and Figure 7.
695
696

697 Another key aspect to highlight from Figure 9-(a) is the
698 appearance of humps in Stage C for all three cases (circled in orange),
699 which can be indicative of the occurrence of dispersed interfacial
700 structure formation, either from recurring ligament production or large
701 coalesced drop fragmentation, as explored in Section 3.2.3. Eventually,
702 the rate of drop formation and coalescence seems to stabilise
703 somewhat, with a steady decline in the number of drops and smaller
704 rates for the clean and Marangoni-free cases after $t = 28 \times Rev.$
705 compared to the onset of Stage C. From this point onward, the
706 dynamics developing in the tank stagnate, reducing to sporadic
707 coalescence and subsequent breakup chains as described in Section
708 3.2.3. For this reason, the simulations were terminated after this
709 point.
710

711 Finally, the dispersed entities number at the instant where we
712 terminated our simulations takes the following order: surfactant-

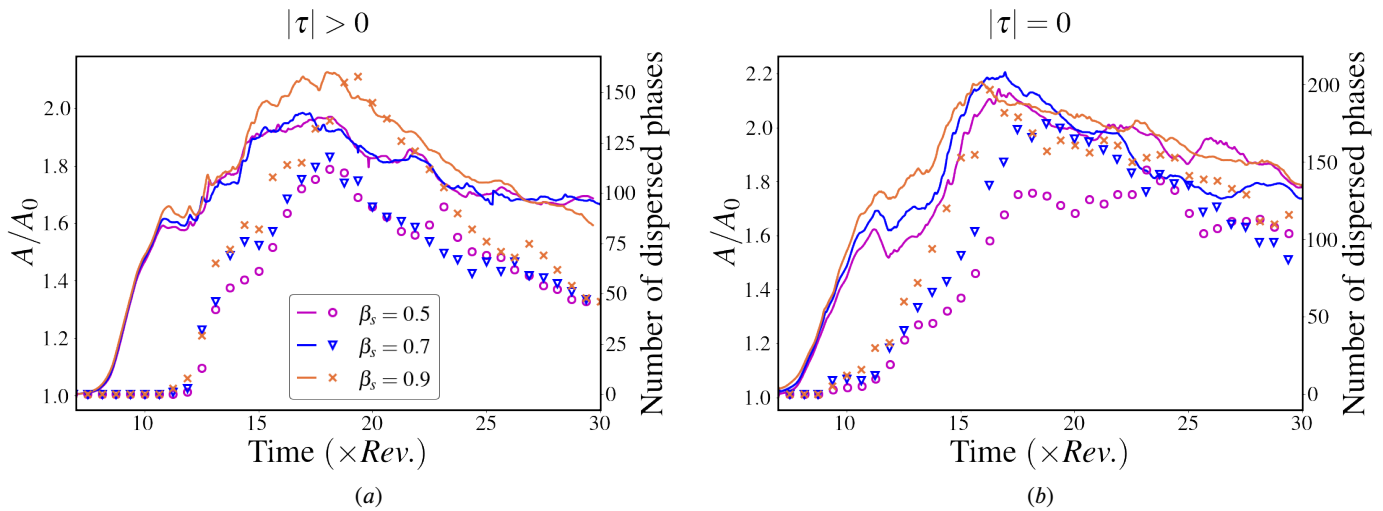


Figure 10: A general quantitative insight into the mixing process for the systems with Marangoni stress turned on (a) and off (b), with regard to the evolution of interfacial area (lines) and dispersed entities count (symbols). Profiles of both metrics are displayed for varying surfactant elasticity numbers $\beta_s = 0.5, 0.7, 0.9$ during $t = 7 - 30 \times Rev.$. Except for the variations in β_s , the rest of the surfactant-related parameters remain unchanged from Figure 3.

free (17), surfactant-laden I (43), and surfactant-laden II (82) systems. This provides further indication of the surfactant effect on the liquid dispersion in the studied configuration as summarised below:

- The reduced interfacial tension promotes tip-streaming (or tip-dropping), which contributes to the formation of more dispersed drops in the surfactant-laden I system;
- The Marangoni stress, in general, acts to counteract and retard interfacial deformation and drop formation, which explains the larger dispersed phases number in its absence;
- Marangoni stress is found to encourage breakup events via the capillary instability, which is commonly occurs under general emulsion scenarios [Janssen and Meijer, 1993], and, to some extent, suppresses tip-streaming.

3.3.2. Drop size distribution

The dispersed entities number alone is not a representative metric of the effect of surfactant in the stirred mixer. Additionally, a drop size distribution analysis at $t = 26 \times Rev.$ is carried out for the three studied cases herein, as presented in Figure 9-(b). The drop size in this context is defined as the volume of a dispersed entity, V_d , and is normalised by the volume of a spherical drop, V_{cap} , whose diameter corresponds to the capillary length scale, $\sqrt{\sigma_s(\rho_w - \rho_o)g}$.

The data structure has been evaluated using quantile-quantile (Q-Q) test and box plots, and the outliers (i.e., non-physical tiny drops and elongating large ligaments) are removed from the analysis. In the field of statistics, one commonly applies the Kolmogorov-Smirnoff (K-S) test [Massey Jr, 1951] and the Anderson-Darling (A-D) test [Anderson and Darling, 1954] to examine the goodness of one population of

data to fit one specific distribution; a non-parametric analysis of variance, for example, Kruskal-Wallis (K-W) test [Kruskal and Wallis, 1952] is then used to contrast the distributions and the following Dunn's test [Dunn, 1961, 1964] specifies the distinct sets of data. Following such procedure, the filtered data sets are fitted to a logistic distribution, satisfying both the K-S test and the A-D test with a significance level of 0.05. Furthermore, K-W test is conducted to contrast the distributions, where statistical significance is implied among the three data sets. More specifically, subsequent Dunn's test determines that the Marangoni-free system is distinct from (lower than) the other two systems, as far as their medians are concerned. This finding is consistent with the prior work [Padron, 2004] pointing out the manifold effect of surfactant on the average drop size, especially in mixing scenarios, as opposed to the assertion that the addition of surfactant simply reduces the interfacial tension, and therefore, the dispersed drop size. The deviation for the Marangoni-free data strengthens this statement indicating that the effect of surfactant on the drop size is not limited to lowering interfacial tension but also arises from the Marangoni stress, which plays a role in drop breakup mechanisms as demonstrated in previous sections.

Moreover, skewness and kurtosis are computed to examine the asymmetry (i.e., tail) of the distributions. First, negative skewness for all three cases signifies the left-tailed shape, which can be translated as all three cases exhibit an inclination to produce small drops. In regard to the magnitude (absolute value) of skewness, incremental skewness is obtained for the three cases following the order: surfactant-free (-0.23) < surfactant-laden I (-0.76) < surfactant-laden II (-1.01). In addition, the kurtosis indicates "heavier" tails for the same ordering, in other words, the surfactant-laden II system produces the largest amount of small drops, followed by the surfactant-laden I, and finally the surfactant-free

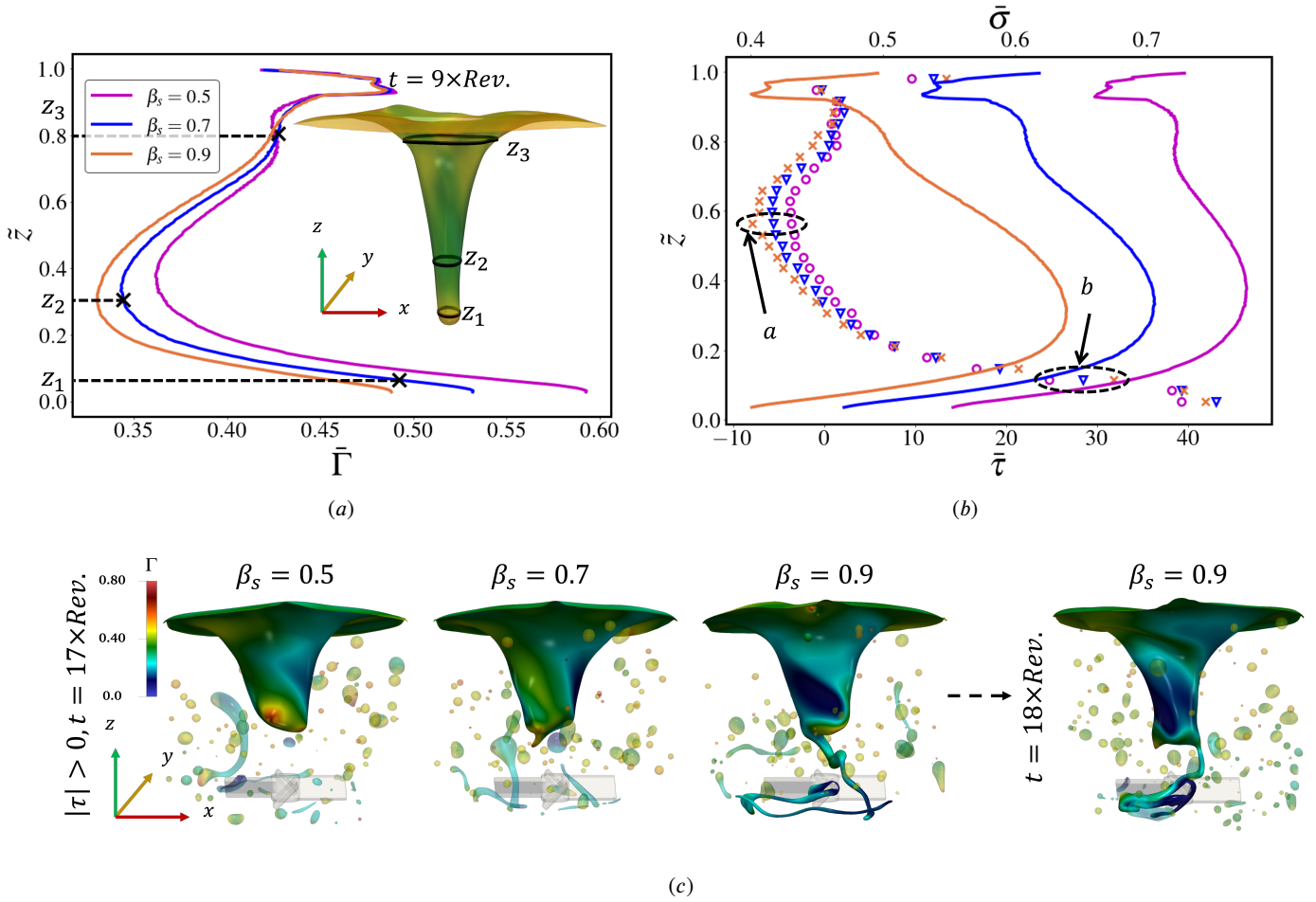


Figure 11: The averaged surfactant properties along the interface at $t = 9 \times Rev.$, (a) the averaged surfactant concentration, $\bar{\Gamma}$; (b) the averaged interfacial tension ($\bar{\sigma}$, lines) and the averaged magnitude of Marangoni stresses ($\bar{\tau}$, symbols). The \bar{z} refers to the dimensionless height on the interface, scaled using the minimum position of the deforming interface as in Figure 4; here, negative τ represents its direction pointing downward. (c) A comparison of the interfacial shapes for the three systems in the presence of Marangoni stress at $t = 17 \times Rev.$. Except for the β_s variations, the rest of the surfactant-related parameters remain unchanged from Figure 3.

780 system. This comparison leads to a similar conclusion as
 781 above: interfacial tension reduction promotes the production
 782 of smaller drops while the Marangoni stress acts to mitigate
 783 this effect.

784 3.4. Effect of surfactant elasticity, β_s

785 Figure 10-(a) and -(b) provide a quantitative insight into
 786 the mixing process in systems of varying elasticity numbers
 787 with respect to the evolution of the interfacial area (made di-
 788 mensionless via the initial interfacial area, A_0) and dispersed
 789 phases count; (a) refers to the three cases with Marangoni
 790 stress turned on and (b) presents the Marangoni-free sys-
 791 tems. It can be seen that prior to dispersed entity forma-
 792 tion (i.e., Stage A defined in Section 3.3.1), a small change in in-
 793 terfacial area is seen for both Marangoni-free system and its
 794 counterpart in the presence of Marangoni stress. This is con-
 795 sistent with what we demonstrated in Section 3.2.1 that the
 796 elongational flow experienced by the deforming interface is
 797 so strong that the effect of increasing β_s (and therefore the

modified interfacial tension and Marangoni stress) is neg-
 798 ligible during this step. After that, increasing β_s , which
 799 augments the sensitivity of interfacial tension to the surfac-
 800 tant concentration, generally promotes interface deformation and
 801 formation of dispersed entities (shown as incremental A/A_0
 802 and entities count, respectively, in Figure 10-(b)). However,
 803 these effects are only prominent prior to the fall-off (i.e.,
 804 Stage C defined in Section 3.3.1). Following the onset of
 805 the fall-off, no distinguishable trend regarding either the in-
 806 terfacial area or dispersed entities count is seen for increas-
 807 ing β_s . Furthermore, in comparison with Figure 10-(a), the
 808 presence of Marangoni stress mitigates the effects mentioned
 809 above. In other words, under realistic scenarios, increasing
 810 β_s from 0.5 to 0.7 leads to insignificant change in interfacial
 811 area and dispersed phases count. Instead, an obvious in-
 812 crease is seen in both metrics at $t = 15 - 25 \times Rev.$ for
 813 $\beta_s = 0.9$, the largest β_s studied herein.
 814

To elucidate the observations highlighted above, Figure 11
 815 provides a comparison ($t = 9 \times Rev.$) among the three cases
 816

with Marangoni stress turned on in terms of surfactant-related properties on the interface. First, to gain a comprehensive insight into the surfactant property profile on the deforming interface, a quantity (for instance, the surfactant concentration Γ), is averaged over a horizontal slice of the interface. The averaged Γ , $\bar{\Gamma}$, on a sequence of horizontal slices, located at different heights of the interface, is then tracked. This gives Figure 11-(a) where the markers refer to the $\bar{\Gamma}$ over the horizontal slice at the corresponding height, as demonstrated in the schematic inset. Similarly, Figure 11-(b) plots the averaged interfacial tension and the strength of Marangoni stresses along the interface (vertically). From these figures, larger β_s results in lower interfacial tension, as expected, more uniform surfactant concentration (narrower range of $\bar{\Gamma}$), and larger Marangoni stress induced along the interface. As shown in the figure, the Marangoni stress on the waist of the interface (labeled as a , $\bar{z} \approx 0.6$) is larger in magnitude augmenting deformation (negative, pointing downward); likewise, that induced in the lower part of the interface (labeled as b , $\bar{z} \approx 0.1$) is stronger retarding deformation (positive, pointing upward). Meanwhile, the retarding force exceeds the augmenting one (take $\beta_s = 0.9$ as an example, $|\tau|_b \approx 32 > |\tau|_a \approx 9$). Hence, the sum of these effects is reflected as a negligible change in interfacial area (i.e., overlapping lines) as observed in Figure 10.

The ensuing Figure 11-(c) provides a comparison of the interfacial shapes for the three cases in the presence of Marangoni stress illustrating the cause of the significant increase in interfacial area and dispersed entities count for $\beta_s = 0.9$. As shown in this figure, while the deforming interfaces in the other two cases start to retract and detach the impeller hub ($t = 17 \times Rev.$), the $\beta_s = 0.9$ case exhibits an interface in the shape of a tail extending to the vessel bottom. Several long stretching ligaments are also generated, which subsequently give way to multiple dispersed drops leading to a sharp increase in dispersed drop count. Such phenomenon lasts until $t = 18 \times Rev.$. On the other hand, this feature is missing for the Marangoni-free system. This provides further indication that one of the effects exerted by Marangoni stress is to encourage drop breakup via long ligament fragmentation driven by the capillary instability (see Section 3.2.2).

From above, the effect of β_s is best appreciated during the intermediate period of the mixing process, which corresponds to Steps 2 and 3 of the interfacial behaviours defined in Section 3.1. After the cessation of the interface-impeller contact, the effect of changing surfactant elasticity diminishes as displayed in the plots at the instant where we terminated our simulations; the cases associated with the three studied β_s produce similar interfacial area and dispersed entity count, for both the scenarios with Marangoni stress turned on and off. This implies that the effect of changing β_s is more pronounced on drop dispersion compared to coalescence. It should be noted, however, that due to the complex nature of the flow considered in the present work, larger computational resolution is required to recover the potential (and subtle) effect of surfactant on drop coalescence, which is beyond the discussion presented herein.

4. Conclusions

The current study has extended our previous work on numerical analysis regarding oil-water emulsification inside an un-baffled stirred vessel by accounting for the presence of soluble surfactant. We have contrasted the surfactant-free and surfactant-laden systems in terms of interfacial behaviors during mixing, transient number of dispersed phases, and drop size distribution at the instant where the simulations are terminated. Furthermore, our simulations allow us to turn off the Marangoni stress, which is evidently unachievable in experimental work. In this way, we have isolated the effects that arise from interfacial tension reduction and the Marangoni stress induced by surfactant concentration gradient. In general, the decrease in interfacial tension eases the interface deformation and drop formation in our system, promoting a second drop breakup mechanism, the tip-streaming/dropping, which is not observed in surfactant-free system. On the other hand, the role played by the Marangoni stresses is dependent on the local surfactant concentration distribution. In particular, it could either encourage breakup events via a capillary instability, or retard interfacial elongation and thereby drop production, especially via tip-streaming. From the perspective of drop size, the presence of surfactant exerts manifold effects such that lowering interfacial tension aids the production of smaller drops, while the Marangoni stress mitigates this influence.

In addition, a parametric study has been performed to address the effect of surfactant elasticity, β_s . We have demonstrated that increasing β_s facilitates interface deformation and thereby drop formation by decreasing the average interfacial tension. However, the presence of Marangoni stress counteracts these effects and leads to a sharp increase in both interfacial area and dispersed phases count for the largest β_s ($\beta_s = 0.9$) during $t = 15 - 20 \times Rev.$, by encouraging the formation of long ligaments (and thereby subsequent drop production). Ultimately, the deviation vanishes at the instant we terminated the simulations where similar drop number and interfacial area are observed.

Throughout this work, we have provided a detailed insight into surfactant-laden interfacial dynamics within a practical operation unit, i.e., the stirred vessel. Though all the results are from a specific configuration, the physics we have discussed is generic to stirred mixers. Considering the flexibility provided by our simulations, our future work will address other surfactant properties including diffusion and sorption kinetics. We will also use our high-fidelity simulations to produce correlations of the drop size distributions with the dimensionless parameters that characterise our surfactant system.

Acknowledgements

This work is supported by the Engineering and Physical Sciences Research Council, United Kingdom, through the EPSRC MEMPHIS (EP/K003976/1) and PREMIERE (EP/T000414/1) Programme Grants. O.K.M. acknowledges funding from PETRONAS and the Royal Academy of Engineering for a Research Chair in Multiphase Fluid Dynamics. We acknowledge HPC facilities provided by the Re-

930 search Computing Service (RCS) of Imperial College Lon-
 931 don for the computing time. D.J. and J.C. acknowledge sup-
 932 port through HPC/AI computing time at the Institut du De-
 933 veloppement et des Ressources en Informatique Scientifique
 934 (IDRIS) of the Centre National de la Recherche Scientifique
 935 (CNRS), coordinated by GENCI (Grand Equipement Na-
 936 tional de Calcul Intensif) Grant 2023 A0142B06721.

937 References

938 Theodore W Anderson and Donald A Darling. A test of goodness of fit.
 939 *Journal of the American statistical association*, 49(268):765–769, 1954.
 940 Kartik Arora, Radhakrishna Sureshkumar, Matthew P Scheiner, and
 941 Justin L Piper. Surfactant-induced effects on turbulent swirling flows.
 942 *Rheologica acta*, 41(1):25–34, 2002.
 943 Assen Batchvarov, Lyes Kahouadji, Mirco Magnini, Cristian R Constante-
 944 Amores, S Shin, J Chergui, D Juric, RV Craster, and Omar K Matar. Ef-
 945 fect of surfactant on elongated bubbles in capillary tubes at high reynolds
 946 number. *Physical Review Fluids*, 5(9):093605, 2020.
 947 Assen Batchvarov, Lyes Kahouadji, Cristian R Constante-Amores,
 948 Gabriel F Norões Gonçalves, S Shin, J Chergui, D Juric, RV Craster,
 949 and Omar K Matar. Three-dimensional dynamics of falling films in the
 950 presence of insoluble surfactants. *J. Fluid. Mech.*, 906:A16, 2021.
 951 Ivan B Bazhlekov, Patrick D Anderson, and Han EH Meijer. Numerical in-
 952 vestigation of the effect of insoluble surfactants on drop deformation and
 953 breakup in simple shear flow. *Journal of colloid and interface science*,
 954 298(1):369–394, 2006.
 955 BJ Briscoe, CJ Lawrence, and WGP Mietus. A review of immiscible fluid
 956 mixing. *Advances in Colloid and Interface Science*, 81(1):1–17, 1999.
 957 A Busciglio, F Grisafi, F Scargiali, and A Brucato. Mixing dynamics in
 958 uncovered unbaffled stirred tanks. *Chemical Engineering Journal*, 254:
 959 210–219, 2014.
 960 A Busciglio, F Scargiali, F Grisafi, and A Brucato. Oscillation dynamics
 961 of free vortex surface in uncovered unbaffled stirred vessels. *Chemical
 962 Engineering Journal*, 285:477–486, 2016.
 963 Chien-Hsiang Chang and Elias I Franses. Adsorption dynamics of surfac-
 964 tants at the air/water interface: a critical review of mathematical models,
 965 data, and mechanisms. *Colloids and Surfaces A: Physicochemical and
 966 Engineering Aspects*, 100:1–45, 1995.
 967 Eleni G Chatzi, Costas J Boutris, and Costas Kiparissides. On-line monitor-
 968 ing of drop size distributions in agitated vessels. 1. effects of temperature
 969 and impeller speed. *Industrial & engineering chemistry research*, 30(3):
 970 536–543, 1991.
 971 Hong Bai Chin and Chang Dae Han. Studies on droplet deformation and
 972 breakup. ii. breakup of a droplet in nonuniform shear flow. *Journal of
 973 rheology*, 24(1):1–37, 1980.
 974 CR Constante-Amores, L Kahouadji, A Batchvarov, S Shin, J Chergui,
 975 Damir Juric, and OK Matar. Dynamics of retracting surfactant-laden
 976 ligaments at intermediate ohnesorge number. *Phys. Rev. Fluids*, 5, 2020.
 977 CR Constante-Amores, A Batchvarov, L Kahouadji, S Shin, J Chergui,
 978 Damir Juric, and OK Matar. Role of surfactant-induced marangoni
 979 stresses in drop-interface coalescence. *Journal of Fluid Mechanics*, 925,
 980 2021a.
 981 CR Constante-Amores, T Abadie, L Kahouadji, S Shin, J Chergui, D Jur-
 982 ic, AA Castrejon-Pita, and OK Matar. Direct numerical simulations of
 983 turbulent jets: vortex–interface–surfactant interactions. *Journal of Fluid
 984 Mechanics*, 955:A42, 2023.
 985 Cristian R Constante-Amores, Lyes Kahouadji, Assen Batchvarov, Seung-
 986 won Shin, Jalel Chergui, Damir Juric, and Omar K Matar. Dynamics of
 987 a surfactant-laden bubble bursting through an interface. *Journal of Fluid
 988 Mechanics*, 911, 2021b.
 989 James W Deardorff. A numerical study of three-dimensional turbulent
 990 channel flow at large reynolds numbers. *Journal of Fluid Mechanics*,
 991 41(2):453–480, 1970.
 992 Chengdi Dong, Ching-Tien Hsu, Chin-Yuan Chiu, and Shi-Yow Lin. A
 993 study on surfactant adsorption kinetics: Effect of bulk concentration

on the limiting adsorption rate constant. *Langmuir*, 16(10):4573–4580,
 2000. 994
 995
 996 Olive Jean Dunn. Multiple comparisons among means. *Journal of the
 997 American statistical association*, 56(293):52–64, 1961.
 998
 999 Olive Jean Dunn. Multiple comparisons using rank sums. *Technometrics*,
 6(3):241–252, 1964.
 1000
 1001 Charles D Eggleton and Kathleen J Stebe. An adsorption–desorption-
 1002 controlled surfactant on a deforming droplet. *Journal of colloid and
 1003 interface science*, 208(1):68–80, 1998.
 1004
 1005 Charles D Eggleton, Yashodhara P Pawar, and Kathleen J Stebe. Insoluble
 1006 surfactants on a drop in an extensional flow: a generalization of the stag-
 1007 nated surface limit to deforming interfaces. *Journal of Fluid Mechanics*,
 385:79–99, 1999.
 1008
 1009 Charles D Eggleton, Tse-Min Tsai, and Kathleen J Stebe. Tip streaming
 1010 from a drop in the presence of surfactants. *Physical review letters*, 87
 1011 (4):048302, 2001.
 1012
 1013 Amer El-Hamouz. Effect of surfactant concentration and operating temper-
 1014 ature on the drop size distribution of silicon oil water dispersion. *Journal
 1015 of Dispersion Science and Technology*, 28(5):797–804, 2007.
 1016
 1017 E. A. Fadlun, R. Verzicco, P. Orlandi, and J. Mohd-Yusof. Combined
 1018 immersed-boundary finite-difference methods for three-dimensional
 1019 complex flow simulations. *J. Comp. Phys.*, 161:35–60, 2000.
 1020
 1021 Ying Fan, Jiao Sun, Jie Jin, Hui Zhang, and Wenyi Chen. The effect of baffle
 1022 on flow structures and dynamics stirred by pitch blade turbine. *Chemical
 1023 Engineering Research and Design*, 168:227–238, 2021.
 1024
 1025 Kathleen Feigl, David Megias-Alguacil, Peter Fischer, and Erich J Wind-
 1026 hab. Simulation and experiments of droplet deformation and orientation
 1027 in simple shear flow with surfactants. *Chemical engineering science*, 62
 1028 (12):3242–3258, 2007.
 1029
 1030 Peter Fischer and Philipp Erni. Emulsion drops in external flow fields—the
 1031 role of liquid interfaces. *Current Opinion in Colloid & Interface Science*,
 12(4-5):196–205, 2007.
 1032
 1033 Tanya Goloub and Robert J Pugh. The role of the surfactant head group in
 1034 the emulsification process: Single surfactant systems. *Journal of colloid
 1035 and interface science*, 257(2):337–343, 2003.
 1036
 1037 Harold P Grace. Dispersion phenomena in high viscosity immiscible fluid
 1038 systems and application of static mixers as dispersion devices in such
 1039 systems. *Chemical Engineering Communications*, 14(3-6):225–277,
 1040 1982.
 1041
 1042 F Groeneweg, F Van Dieren, and WGM Agterof. Droplet break-up in a
 1043 stirred water-in-oil emulsion in the presence of emulsifiers. *Colloids
 1044 and Surfaces A: Physicochemical and Engineering Aspects*, 91:207–
 1045 214, 1994.
 1046
 1047 Andreas Håkansson, Peyman Olad, and Fredrik Innings. Identification and
 1048 mapping of three distinct breakup morphologies in the turbulent inertial
 1049 regime of emulsification—effect of weber number and viscosity ratio.
 1050 *Processes*, 10(11):2204, 2022.
 1051
 1052 Yunfei He, Pavel Yazhgor, Anniina Salonen, and Dominique Langevin.
 1053 Adsorption–desorption kinetics of surfactants at liquid surfaces.
 1054 *Advances in colloid and interface science*, 222:377–384, 2015.
 1055
 1056 Julius O Hinze. Fundamentals of the hydrodynamic mechanism of splitting
 1057 in dispersion processes. *AIChE journal*, 1(3):289–295, 1955.
 1058
 1059 JIM Janssen, A Boon, and WGM Agterof. Influence of dynamic interfacial
 1060 properties on droplet breakup in simple shear flow. *AIChE journal*, 40
 1061 (12):1929–1939, 1994.
 1062
 1063 JMH Janssen and HEH Meijer. Droplet breakup mechanisms: Stepwise
 1064 equilibrium versus transient dispersion. *Journal of Rheology*, 37(4):
 1065 597–608, 1993.
 1066
 1067 Thomas RN Jansson, Martin P Haspang, Kåre H Jensen, Pascal Hersen,
 1068 and Tomas Bohr. Polygons on a rotating fluid surface. *Physical review
 1069 letters*, 96(17):174502, 2006.
 1070
 1071 Fang Jin and Kathleen J Stebe. The effects of a diffusion controlled surfac-
 1072 tant on a viscous drop injected into a viscous medium. *Physics of Fluids*,
 19(11):112103, 2007.
 1073
 1074 Fang Jin, Nivedita R Gupta, and Kathleen J Stebe. The detachment of a
 1075 viscous drop in a viscous solution in the presence of a soluble surfactant.
 1076 *Physics of Fluids*, 18(2):022103, 2006.
 1077
 1078 Lyes Kahouadji and L Martin Witkowski. Free surface due to a flow driven

- 1062 by a rotating disk inside a vertical cylindrical tank: axisymmetric con- 1130
 1063 figuration. *Physics of Fluids*, 26(7):072105, 2014. 1131
 1064 Lyes Kahouadji, Fuyue Liang, Juan P Valdes, Seungwon Shin, Jalel Cher- 1132
 1065 gui, Damir Juric, Richard V Craster, and Omar K Matar. The transition 1133
 1066 to aeration in turbulent two-phase mixing in stirred vessels. *Flow*, 2: 1134
 1067 E30, 2022. 1135
 1068 Pritish M Kamat, Brayden W Wagoner, Sumeet S Thete, and Osman A 1136
 1069 Basaran. Role of marangoni stress during breakup of surfactant-covered 1137
 1070 liquid threads: reduced rates of thinning and microthread cascades. 1138
 1071 *Physical Review Fluids*, 3(4):043602, 2018. 1139
 1072 Abraham Koshy, TR Das, and R Kumar. Effect of surfactants on drop break- 1140
 1073 age in turbulent liquid dispersions. *Chemical engineering science*, 43(3): 1141
 1074 649–654, 1988. 1142
 1075 William H Kruskal and W Allen Wallis. Use of ranks in one-criterion vari- 1143
 1076 ance analysis. *Journal of the American statistical Association*, 47(260): 1144
 1077 583–621, 1952. 1145
 1078 Ronald Laymon. Newton’s bucket experiment. *Journal of the History of* 1146
 1079 *Philosophy*, 16(4):399–413, 1978. 1147
 1080 James M Lee and Yee Soong. Effects of surfactants on the liquid-liquid dis- 1148
 1081 persions in agitated vessels. *Industrial & Engineering Chemistry Process* 1149
 1082 *Design and Development*, 24(1):118–121, 1985. 1150
 1083 Andrei A Levchenko, Brian P Argo, Ruxandra Vidu, Raisa V Talroze, and 1151
 1084 Pieter Stroeve. Kinetics of sodium dodecyl sulfate adsorption on and 1152
 1085 desorption from self-assembled monolayers measured by surface plas- 1153
 1086 mon resonance. *Langmuir*, 18(22):8464–8471, 2002. 1154
 1087 Liangchao Li, Jiajun Wang, Lianfang Feng, and Xueping Gu. Computa- 1155
 1088 tional fluid dynamics simulation of hydrodynamics in an uncovered 1156
 1089 un baffled tank agitated by pitched blade turbines. *Korean Journal of* 1157
 1090 *Chemical Engineering*, 34(11):2811–2822, 2017. 1158
 1091 Xiaofan Li and C Pozrikidis. The effect of surfactants on drop deformation 1159
 1092 and on the rheology of dilute emulsions in stokes flow. *Journal of fluid* 1160
 1093 *mechanics*, 341:165–194, 1997. 1161
 1094 Fuyue Liang, Lyes Kahouadji, Juan Pablo Valdes, Seungwon Shin, Jalel 1162
 1095 Chergui, Damir Juric, and Omar K Matar. Numerical study of oil-water 1163
 1096 emulsion formation in stirred vessels: effect of impeller speed. *Flow*, 2: 1164
 1097 E34, 2022. 1165
 1098 Douglas K Lilly. The representation of small-scale turbulence in numerical 1166
 1099 simulation experiments. *IBM Form*, pages 195–210, 1967. 1167
 1100 Douglas Keith Lilly. On the application of the eddy viscosity concept in the 1168
 1101 inertial sub-range of turbulence. *NCAR manuscript*, 123, 1966. 1169
 1102 EH Lucassen-Reynders and KA Kuijpers. The role of interfacial properties 1170
 1103 in emulsification. *Colloids and Surfaces*, 65(2-3):175–184, 1992. 1171
 1104 Harishankar Manikantan and Todd M Squires. Surfactant dynamics: hid- 1172
 1105 den variables controlling fluid flows. *Journal of fluid mechanics*, 892: 1173
 1106 P1, 2020. 1174
 1107 Frank J Massey Jr. The kolmogorov-smirnov test for goodness of fit. *Journal* 1175
 1108 *of the American statistical Association*, 46(253):68–78, 1951. 1176
 1109 Paul Mavros, Alain Ricard, Catherine Xuereb, and Joel Bertrand. A study of 1177
 1110 the effect of drag-reducing surfactants on flow patterns in stirred vessels. 1178
 1111 *Chemical Engineering Research and Design*, 89(1):94–106, 2011. 1179
 1112 Oden J McMillan and Joel H Ferziger. Direct testing of subgrid-scale mod- 1180
 1113 els. *Aiaa Journal*, 17(12):1340–1346, 1979. 1181
 1114 Johan Meyers and Pierre Sagaut. On the model coefficients for the standard 1182
 1115 and the variational multi-scale smagorinsky model. *Journal of Fluid* 1183
 1116 *Mechanics*, 569:287–319, 2006. 1184
 1117 William J Milliken and L Gary Leal. The influence of surfactant on the 1185
 1118 deformation and breakup of a viscous drop: The effect of surfactant sol- 1186
 1119 ubility. *Journal of Colloid and Interface Science*, 166(2):275–285, 1994. 1187
 1120 WJ Milliken, Howard A Stone, and LG Leal. The effect of surfactant on 1188
 1121 the transient motion of newtonian drops. *Physics of Fluids A: Fluid* 1189
 1122 *Dynamics*, 5(1):69–79, 1993. 1190
 1123 VP Mishra, P Kumar, and JB Joshi. Flow generated by a disc turbine in 1191
 1124 aqueous solutions of polyacrylamide. *Chemical Engineering Journal*, 1192
 1125 71(1):11–21, 1998. 1193
 1126 J. Mohd-Yusof. Combined immersed-boundary / b-spline methods for sim- 1194
 1127 ulations of flow in complex geometries. *Center for Turbulence Research* 1195
 1128 *Annual Research Briefs*, pages 317–327, 1997. 1196
 1129 Giuseppina Montante, Fabio Laurenzi, Alessandro Paglianti, and Franco 1197
 Magelli. A study on some effects of a drag-reducing agent on the perfor- 1198
 mance of a stirred vessel. *Chemical Engineering Research and Design*, 1199
 89(11):2262–2267, 2011. 1200
 Gustavo A Padron. Effect of surfactants on drop size distributions in a batch, 1201
 rotor-stator mixer. PhD thesis, 2004. 1202
 Rennan Pan, John Green, and Charles Maldarelli. Theory and experiment 1203
 on the measurement of kinetic rate constants for surfactant exchange at 1204
 an air/water interface. *Journal of colloid and interface science*, 205(2): 1205
 213–230, 1998. 1206
 Edward L Paul, Victor A Atiemo-Obeng, and Suzanne M Kresta. *Handbook* 1207
of industrial mixing. Wiley Online Library, 2004. 1208
 Anthony E Perry and Min S Chong. A description of eddying motions 1209
 and flow patterns using critical-point concepts. *Annual Review of Fluid* 1210
Mechanics, 19(1):125–155, 1987. 1211
 Stephen B Pope. Ten questions concerning the large-eddy simulation of 1212
 turbulent flows. *New journal of Physics*, 6(1):35, 2004. 1213
 J Ratulowski and H-C Chang. Marangoni effects of trace impurities on the 1214
 motion of long gas bubbles in capillaries. *Journal of Fluid Mechanics*, 1215
 210:303–328, 1990. 1216
 A. W. Russell, L. Kahouadji, K. Mirpuri, A. Quarmby, P. M. Piccione, O. K. 1217
 Matar, P. F. Luckham, and C. N. Markides. Mixing viscoplastic fluids in 1218
 stirred vessels over multiple scales: A combined experimental and cfd 1219
 approach. *Chem. Eng. Sci.*, 208:115129, 2019. 1220
 Hermann Schlichting and Joseph Kestin. *Boundary layer theory*, volume 1221
 121. Springer, 1961. 1222
 Seungwon Shin, Jalel Chergui, and Damir Juric. A solver for massively 1223
 parallel direct numerical simulation of three-dimensional multiphase 1224
 flows. *Journal of Mechanical Science and Technology*, 31(4):1739– 1225
 1751, 2017. 1226
 Seungwon Shin, Jalel Chergui, Damir Juric, Lyes Kahouadji, Omar K 1227
 Matar, and Richard V Craster. A hybrid interface tracking–level set 1228
 technique for multiphase flow with soluble surfactant. *Journal of* 1229
Computational Physics, 359:409–435, 2018. 1230
 Giovanni Soligo, Alessio Roccon, and Alfredo Soldati. Breakage, coales- 1231
 cence and size distribution of surfactant-laden droplets in turbulent flow. 1232
Journal of Fluid Mechanics, 881:244–282, 2019. 1233
 Giovanni Soligo, Alessio Roccon, and Alfredo Soldati. Deformation of 1234
 clean and surfactant-laden droplets in shear flow. *Meccanica*, 55(2): 1235
 371–386, 2020a. 1236
 Giovanni Soligo, Alessio Roccon, and Alfredo Soldati. Effect of surfactant- 1237
 laden droplets on turbulent flow topology. *Physical Review Fluids*, 5(7): 1238
 073606, 2020b. 1239
 Howard A Stone and L Gary Leal. The effects of surfactants on drop defor- 1240
 mation and breakup. *Journal of Fluid Mechanics*, 220:161–186, 1990. 1241
 Georgios H Vatistas. A note on liquid vortex sloshing and kelvin’s equilib- 1242
 ria. *Journal of Fluid Mechanics*, 217:241–248, 1990. 1243
 H Wu and GK Patterson. Laser-doppler measurements of turbulent-flow 1244
 parameters in a stirred mixer. *Chemical engineering science*, 44(10): 1245
 2207–2221, 1989. 1246